

Building three-dimensional differentiable manifolds numerically



Lee Lindblom^{a,b,*}, Oliver Rinne^c, Nicholas W. Taylor^d

^a Center for Astrophysics and Space Sciences, University of California at San Diego, 9500 Gilman Drive, La Jolla, CA 92093, USA

^b Center for Computational Mathematics, University of California at San Diego, 9500 Gilman Drive, La Jolla, CA 92093, USA

^c Faculty 4, HTW Berlin – University of Applied Sciences, Treskowallee 8, 10318 Berlin, Germany

^d Department of Physics, Cornell University, Ithaca, NY 14853, USA

ARTICLE INFO

Article history:

Received 10 July 2021

Received in revised form 15 November 2021

Accepted 5 January 2022

Available online 11 January 2022

Keywords:

Three-dimensional differentiable manifolds

Numerical methods

Biharmonic equation

Hantzsche-Wendt space

Poincaré dodecahedral space

Seifert-Weber space

ABSTRACT

A method is developed here for building differentiable three-dimensional manifolds on multicube structures. This method constructs a sequence of reference metrics that determine differentiable structures on the cubic regions that serve as non-overlapping coordinate charts on these manifolds. It uses solutions to the two- and three-dimensional biharmonic equations in a sequence of steps that increase the differentiability of the reference metrics across the interfaces between cubic regions. This method is algorithmic and has been implemented in a computer code that automatically generates these reference metrics. Examples of three-manifolds constructed in this way are presented here, including representatives from five of the eight Thurston geometrization classes, plus the well-known Hantzsche-Wendt, the Poincaré dodecahedral space, and the Seifert-Weber space.

© 2022 The Author(s). Published by Elsevier Inc. This is an open access article under the CC BY license (<http://creativecommons.org/licenses/by/4.0/>).

1. Introduction

Differentiable manifolds are the mathematical structures on which the differential equations of the physical sciences are solved to provide descriptions of the universe as we understand it. This paper develops methods that allow these equations to be solved numerically in a convenient way on a much broader class of manifolds.

In the traditional literature, an n -dimensional differentiable manifold is defined as a space that can be covered by a collection of open sets, plus invertible maps that take each member of this collection onto some open subset of \mathbb{R}^n . In practical terms, these open subsets in \mathbb{R}^n are the coordinate charts used to identify points in the manifold. For points having images in two coordinate patches, the inferred maps in the overlap regions between the patches must be differentiable. The differentiability of these overlap maps defines the differentiable structure of the manifold. This structure is used to define what it means for global tensor fields on the manifold to be continuous and differentiable. The existence of differentiable global tensor fields is fundamental to finding global solutions to the equations of the physical sciences on manifolds. Therefore having, or if necessary creating, a suitably smooth differentiable structure on a manifold is essential.

The traditional description of a differentiable manifold is difficult to implement numerically in a computer code for several reasons: Such an implementation must keep track of the exact size and shape of each coordinate patch in \mathbb{R}^n , plus the exact sizes and shapes of the overlap regions containing points represented in two patches, plus the maps between the

* Corresponding author at: Center for Astrophysics and Space Sciences, University of California at San Diego, 9500 Gilman Drive, La Jolla, CA 92093, USA.
E-mail addresses: llindblom@ucsd.edu (L. Lindblom), oliver.rinne@htw-berlin.de (O. Rinne), nwt2@cornell.edu (N.W. Taylor).

coordinates in the overlap regions. These structures can of course be designed and implemented in a code for any particular manifold. However, each case is unique and each case requires a lot of work to design and implement properly. It requires a great deal of effort even to transform a numerical code designed for use on one manifold into one that can be used on another. In addition, there does not exist in the literature (so far as we know) a catalog containing the needed information (i.e. the needed collections of coordinate regions, plus all the needed information about their overlaps, plus the maps between the overlap regions) that would allow these traditional methods to be implemented in a code in a straightforward way for a broad collection of three-dimensional manifolds.

An alternative description of a differentiable manifold was introduced in Ref. [1] that is simpler in ways that make it more suitable for use in a computer code. In this multicube approach the coordinate charts in \mathbb{R}^n are standardized, requiring each patch to be a cube of uniform coordinate size and orientation. These coordinate patches are chosen not to overlap in \mathbb{R}^n , except for points on the boundaries of the cubes. The global coordinates in \mathbb{R}^n can therefore be used to identify points globally in these manifolds. Since the coordinate patches have uniform sizes and shapes in this approach, the maps that identify points on the boundaries between neighboring patches are particularly simple, consisting of a rigid translation that maps the center of a face into the center of its neighbor's face, followed by a simple rotation (and/or reflection) that aligns the two faces in the appropriate way. In three dimensions, the case of primary interest in this paper, the number of possible rotations/reflections is quite small (just 48), so all the possible maps are easily included in a computer code. It was shown in Ref. [1] that this multicube structure is sufficiently general to represent any two- or three-dimensional manifold in this way.

The simplicity of the structures of the coordinate charts and their overlap regions makes it much easier to implement the multicube description of a manifold in a computer code. In addition, describing manifolds in this way makes it possible to access and easily make use of published catalogs that contain thousands of three-dimensional manifolds represented by their triangulations [2–5]. Some of these catalogs include online access to the explicit triangulations for these manifolds [6]. Converting a triangulation into a multicube structure is straightforward, see e.g. Ref. [1]. A computer code that implements this procedure has been developed as part of this project and is described in some detail in Appendix A. Most of the manifolds included in this study are based on triangulations given in Ref. [6], and then converted to multicube structures by this new code. The basic multicube structures constructed in this way do not come with differentiable structures. So the problem of constructing those differentiable structures—the main focus of this paper—remains.

Since the coordinate patches in a multicube representation do not overlap, it is not possible to construct differentiable structures on these manifolds in the traditional way. Instead, Ref. [1] showed how these structures could be constructed using a reference metric. Given a reference metric that is continuous across each interface boundary in a multicube structure, a simple analytical formula can be used to determine special Jacobians at those boundaries. Those Jacobians can then be used to define what it means for vector and tensor fields to be continuous across those boundaries. A reference metric that is both continuous and differentiable (in the appropriate sense) across the interfaces can also be used to define a covariant derivative that (together with the Jacobians) can be used to determine what it means for vector and tensor fields to be differentiable across those boundaries. This approach was used to construct differentiable structures on a few simple three-dimensional manifolds in Ref. [1]. An algorithmic method for constructing the needed reference metrics numerically for arbitrary two-dimensional manifolds was developed and tested in Ref. [7]. This paper focuses on the more difficult and complicated problem of developing analogous algorithmic methods for constructing reference metrics on arbitrary three-dimensional manifolds.

Most of the equations of the physical sciences require fixing some combination of the values and normal derivatives of the fields at the boundaries of computational domains. This means that a differentiable structure must be present on the manifold that is capable of defining what it means for fields and their derivatives to be continuous across those boundaries. For a manifold constructed by the multicube method, this means that a global C^1 metric is required. The purpose of this paper is to develop a step-by-step algorithm for constructing global C^1 metrics on these manifolds. These steps consist of building a sequence of metrics \hat{g}_{ab} , \tilde{g}_{ab} , \bar{g}_{ab} , and \tilde{g}_{ab} described in detail in Secs. 2 and 3.¹ The first part of this procedure, described in Sec. 2, constructs a global C^0 metric, \hat{g}_{ab} , whose intrinsic parts (i.e., the components that define the intrinsic metric on a given face) are continuous across the interface boundaries between the cubic regions, and which is free from conical singularities at the vertices and along the edges of those regions. The first step, described in Sec. 2.1, re-organizes the multicube structure into a set of overlapping star-shape domains that surround each of the vertices in the multicube structure. Singularity-free flat metrics are constructed on these star-shaped domains in the second step, described in Sec. 2.2. These flat metrics are combined together using a special partition of unity to produce a global C^0 reference metric, \hat{g}_{ab} , in the third step, described in Sec. 2.3.

In Sec. 3 the C^0 metric, \hat{g}_{ab} , is transformed into a C^1 metric \tilde{g}_{ab} in three additional steps. These steps build two additional intermediate metrics, \bar{g}_{ab} and \tilde{g}_{ab} in Secs. 3.1 and 3.2. In the first of these, Sec. 3.1, a conformal transformation is applied to \hat{g}_{ab} that produces a new metric, \bar{g}_{ab} , that makes all the edges of each cubic region into geodesics. This transformation also makes one component of the associated extrinsic curvatures $\tilde{K}_{ab}^{(\alpha)}$ vanish along the edges. The conformal factor needed for this step is produced by solving two-dimensional biharmonic equations on each cube face, with boundary

¹ The notation g_{ab} is often used to represent the physical metric (as determined by solving Einstein's equation for example). To avoid confusion, that notation is not used here in the construction of the C^1 reference metric \tilde{g}_{ab} that is designed only to define the differential structure of the manifold.

conditions along the edges that enforce the geodesic conditions. The pseudo-spectral numerical methods used to solve those equations for this study are described in Appendix B. In Sec. 3.2 gauge transformations are performed on the metric \bar{g}_{ab} at the interfaces of the cubic regions. The resulting metric \tilde{g}_{ab} has the property that its intrinsic components on each cube face are identical to those of \bar{g}_{ab} , but the gauge components of the metric on those faces are deformed in a way that makes all the components of the associated extrinsic curvatures $\tilde{K}_{ab}^{(\alpha)}$ vanish on all the edges of each cubic region. In Sec. 3.3 the metric \tilde{g}_{ab} is adjusted in the interiors of each cubic region (keeping the boundary values fixed) by solving three-dimensional biharmonic equations whose boundary conditions are chosen to make the extrinsic curvatures $\tilde{K}_{ab}^{(\alpha)}$ vanish on each cube face. This \tilde{g}_{ab} retains the continuity of its intrinsic components across each interface boundary inherited from \hat{g}_{ab} and \bar{g}_{ab} . The continuity of the intrinsic metric together with the continuity of the extrinsic curvature are the geometric conditions, often referred to as the Israel junction conditions [8], needed to ensure that the metric \tilde{g}_{ab} is C^1 across the interface boundaries.

Section 4 describes a number of three-dimensional manifolds on which C^1 differentiable structures have been constructed for this study using the methods described in Secs. 2 and 3. Numerical convergence of the Israel junction conditions, the necessary and sufficient conditions that \tilde{g}_{ab} be C^1 across the interface boundaries, is demonstrated for these examples. Appendix D presents detailed multicube structures for a variety of three-dimensional manifolds, including examples from the Thurston geometrization classes [9,10] E^3 , S^3 , $S^2 \times S^1$, $H^2 \times S^1$, and H^3 . The manifolds studied here include 29 that were constructed from triangulations given in Ref. [6] using the code described in Appendix A. In addition a few multicube structures were constructed by hand for several well known three-manifolds: including the Poincaré dodecahedral space [11], Seifert-Weber space [12], and all six compact orientable three-manifolds that admit flat metrics [13,14], including the Hantzsche-Wendt space [15]. Section 5 gives a brief summary of the basic methods developed in this paper and the ways they have been tested numerically. In addition a number of interesting questions and possible extensions of the current results are outlined.

2. Constructing C^0 three-dimensional reference metrics

The procedure to create a continuous (C^0) three-dimensional reference metric, \hat{g}_{ij} , on a multicube structure has three basic steps: In the first, described in Sec. 2.1, the multicube structure is re-organized to create a collection of overlapping star-shaped domains on the manifold. In the second step, described in Sec. 2.2, flat metrics are constructed in each of these overlapping domains. In the third step, described in Sec. 2.3, a global C^0 reference metric, \hat{g}_{ab} , is constructed using these flat metrics and a special partition of unity. Explicit analytic formulas are given in Secs. 2.2 and 2.3 for the C^0 metric, \hat{g}_{ab} , along with the flat metrics and partition of unity functions used to construct it.

All these steps can be, and have been, implemented in a computer code that automatically generates these C^0 metrics using only the multicube structures as input. In the simplest version of this procedure (the one described in most detail here, and the one presently implemented in our code) all the dihedral angles between the cube faces that meet along a particular edge are chosen to have the same size. While this simplifying assumption cannot be applied to most multicube structures, it is general enough that compliant structures have been constructed here on a diverse set of manifolds in Sec. 4 to illustrate these methods.

2.1. Step 1: assembling star-shaped domains

In this first step, the multicube structure consisting of a collection of cubic regions, \mathcal{B}_A , is enhanced by defining a set of domains, called the star-shaped domains, \mathcal{S}_I , that overlap the boundaries between the primary cubic regions. One star-shaped domain surrounds each distinct vertex of the multicube structure. It is constructed from (copies of) all the cubic regions that intersect at that vertex point. (A particular cubic region \mathcal{B}_A may be included more than once in a star-shaped domain if two or more of its vertices are identified with each other.) Each of the star-shaped domains, \mathcal{S}_I , has the topology of an open ball in \mathbb{R}^3 . The index A is used to label the cubes \mathcal{B}_A in the multicube structure, while the index I labels the star-shaped domains \mathcal{S}_I , or equivalently the distinct vertices in the multicube structure. The structures of the individual star-shaped domains depend on the global properties of the multicube structure, in particular on how many cube vertices intersect in the manifold at the center of each \mathcal{S}_I . Fig. 1 illustrates several examples of star-shaped domains having different numbers of cubic regions intersecting at their central vertex points.

A code designed to use multicube structures can be enhanced to assemble the \mathcal{S}_I in a fairly straightforward way: Any multicube structure code must include the cube face identification maps. Starting at one vertex of one cubic region, the identities of the three cubes whose faces are identified with the faces of \mathcal{B}_A adjacent to this vertex are determined from the multicube maps. This can be done, for example, by following the interface identification maps for points near this vertex on each of the three faces that meet at that point. Copies of the three cubes identified as neighbors in this way are added to \mathcal{S}_I . This identification step is repeated for the adjacent faces of each of the additional cubes, and then iterated until (copies of) all the cube vertices that intersect the original vertex point are included in \mathcal{S}_I . Once a star-shaped domain \mathcal{S}_I is complete, if some cube vertices in the full multicube structure remain un-assigned to the center of some star-shaped domain, then a new star-shaped domain \mathcal{S}_{I+1} is constructed around this vertex using the same procedure. The process terminates when all the cube vertices have been included at the center of some star-shaped domain. There are a finite

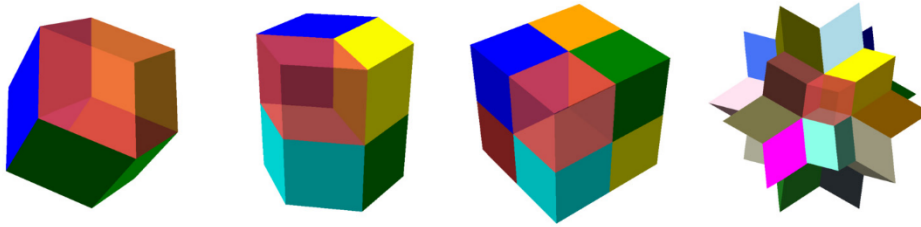


Fig. 1. Examples of star-shaped domains, S_I , in three dimensions consisting of four, six, eight and twenty cubic regions, respectively, that intersect at their central vertex points. The cubic regions in each example have been distorted so they fit together smoothly with the flat metric of the \mathbb{R}^3 in which they are shown. One (red colored) cubic region in each example has been made semi-transparent to allow the internal structures of these domains to be seen more clearly. (For interpretation of the colors in the figure(s), the reader is referred to the web version of this article.)

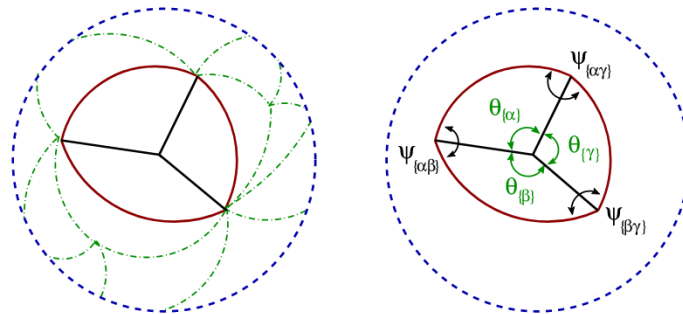


Fig. 2. Left illustration, 2(a), shows the intersection between the corner of a cubic region and a small sphere centered on the vertex of one of the star-shaped domains. This sphere is depicted as the dashed (blue) curve, the intersections between this cubic region and the sphere are shown as solid (red) curves. The dash-dot (green) curves represent the intersections of nearby cubic regions in the star-shaped domain. Right illustration, 2(b), labels the angles that characterize the spherical triangle formed by the intersection of a cubic region and a small sphere centered at its vertex. The $\psi_{(\alpha\beta)}$, etc. are the dihedral angles (in the local flat metric) between the faces of this cubic region. These $\psi_{(\alpha\beta)}$ are also the angles of the spherical triangle. The $\theta_{(\alpha)}$, etc. are the angles between the edges of the cubic region. These $\theta_{(\alpha)}$ are also the arc lengths of the sides of the spherical triangle.

number of cube vertices in any multicube structure (that can be used for practical numerical work), so in practice this process always terminates after a finite number of steps.

2.2. Step 2: constructing semi-local flat metrics

The second step in the procedure to construct global C^0 reference metrics builds a flat metric in each of the star-shaped domains, S_I , introduced in Sec. 2.1. Each S_I consists of a cluster of cubes that intersect at its central point. If these cubes are appropriately distorted into parallelograms (by adjusting the dihedral angles between the cube faces), they can be fitted together (without overlapping and without leaving gaps between them) to form an isometric subset of \mathbb{R}^3 , and thus inherit a natural flat metric. Fig. 1 illustrates several simple examples of star-shaped domains isometrically embedded in \mathbb{R}^3 .

To understand whether the cubic regions of a multicube structure can always be fitted together in this way, consider a small two-sphere surrounding the central vertex of S_I . This sphere intersects all the cubic regions that meet at this central point. The intersections of this sphere with the faces and edges of each cube form triangles on this sphere. Fig. 2(a) illustrates the spherical triangles that result from these intersections. The intersection of one of these cubes, B_A , is displayed as the spherical triangle with solid (red) line edges. The intersections of other nearby cubes in S_I are displayed with dash-dot (green) line edges. Together the intersections from all the cubic regions in S_I form a triangulation of this two-sphere.

Any triangulation on a two-sphere can be realized geometrically in an infinite number of ways. Given any one realization, an infinite number of others can be created simply by moving the vertices of the triangles around on the sphere by small amounts (i.e., much smaller than the sizes of the triangles), and then replacing the edges with geodesics (great circles) between vertices. Each spherical triangle with geodesic edges represents the intersection of a parallelogram (whose dihedral angles match the angles of the triangle) with the two-sphere. Thus there are an infinite number of ways to construct distorted parallelograms that fit together in the correct way to represent S_I as an isometric subset of \mathbb{R}^3 .

An algorithm designed to compute a flat metric on S_I must choose from among the infinite possibilities in some way. Making and implementing that choice is expected to be a complicated optimization problem that we plan to analyze fully in a future study. For the purposes of the present study, however, we have chosen to adopt a simple pragmatic approach: choosing the dihedral angles to have uniform sizes around each edge. This simple approach limits the class of multicube structures to which it can be applied. However, it is general enough that we have been able to construct compliant examples (see Sec. 4) from most of the Thurston geometrization classes, plus examples of several well known manifolds like the

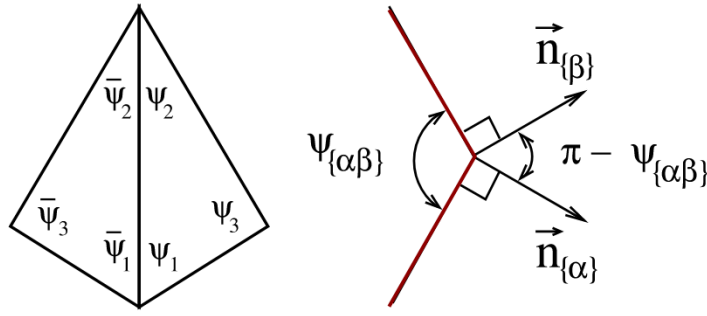


Fig. 3. Left illustration, 3(a), shows two neighboring triangles in a two-sphere triangulation. The uniform dihedral angle assumption requires $\psi_1 = \bar{\psi}_1$ and $\psi_2 = \bar{\psi}_2$, and this in turn implies $\psi_3 = \bar{\psi}_3$ for every pair of neighboring triangles. Right illustration, 3(b), shows the relationship between the dihedral angle $\psi_{\{\alpha\beta\}}$ between two faces of a cubic region, and the angle between the outward directed normals to the cube faces: $\vec{n}_{\{\alpha\}} \cdot \vec{n}_{\{\beta\}} = \cos(\pi - \psi_{\{\alpha\beta\}}) = -\cos(\psi_{\{\alpha\beta\}})$.

Poincaré dodecahedral space [11], Seifert-Weber space [12], and all six compact orientable three-manifolds that admit flat metrics [13,14], including the Hantzsche-Wendt space [15] (also called E6).

Before proceeding with the details of constructing flat metrics on the S_I in these simple multicube structures, it will be helpful to establish some basic notation. The notation $\partial_\alpha \mathcal{B}_A$ (or more compactly $A\{\alpha\}$) is used to refer to the α face of cubic region \mathcal{B}_A . The index α can have the values $\{-x, +x, -y, +y, -z, +z\}$. The edge of region \mathcal{B}_A formed by the intersection of the $A\{\alpha\}$ and $A\{\beta\}$ faces is referred to as $A\{\alpha\beta\}$, and the vertex formed by the intersections of the $A\{\alpha\}$, $A\{\beta\}$, and $A\{\gamma\}$ faces is referred to as $A\{\alpha\beta\gamma\}$. The dihedral angle between the $A\{\alpha\}$ and $A\{\beta\}$ faces is denoted $\psi_{A\{\alpha\beta\}}$, while the angle between the axes at the edges of the $A\{\alpha\}$ face is denoted $\theta_{A\{\alpha\}}$. The $\psi_{A\{\alpha\beta\}}$ are also equal to the angles of the spherical triangle created by the intersection of cube \mathcal{B}_A with a small sphere (see Fig. 2(b)), and the $\theta_{A\{\alpha\}}$ are also equal to the arc lengths of the edges of this triangle.

The uniform dihedral angle spacing assumption adopted here requires the dihedral angles of all the cubic regions that intersect along an edge to be the same. In addition to being reasonably simple to impose, it has the advantage of imposing a rigid uniformity that prevents any cubic region from being more distorted than its neighbors. To prevent conical singularities along the cube edges, the sum of the dihedral angles around each edge must be exactly 2π . The uniform dihedral angle assumption therefore implies that the dihedral angle at the $A\{\alpha\beta\}$ edge must be given by

$$\psi_{A\{\alpha\beta\}} = \frac{2\pi}{K_{A\{\alpha\beta\}}}, \tag{1}$$

where $K_{A\{\alpha\beta\}}$ is the number of cubic regions that intersect along this edge.

The uniform dihedral angle assumption also implies that the triangulations of the two-sphere at the center of a star-shaped domain, S_I , must have a special local reflection symmetry. Fig. 3(a) illustrates two neighboring triangles in one of these triangulations. If the uniform dihedral angle assumption has been imposed then $\psi_1 = \bar{\psi}_1 = 2\pi/K_1$ and $\psi_2 = \bar{\psi}_2 = 2\pi/K_2$. The spherical geometry analog of the angle-side-angle congruence theorem from Euclidean geometry then implies that $\psi_3 = \bar{\psi}_3$. With the uniform dihedral angle assumption, this means that $K_3 = \bar{K}_3$, i.e. the number of edges that meet at vertex 3 in this triangulation must be the same as the number that meet at vertex $\bar{3}$, of the neighboring triangle. This symmetry must apply to every edge of every triangle in the triangulations of the two-spheres at the centers of each star-shaped domain S_I . Therefore, this simple assumption is quite limiting, and is not satisfied by most two-sphere triangulations and consequently most multicube structures.

Any open subset of \mathbb{R}^3 inherits the flat Euclidean metric of \mathbb{R}^3 . Thus any S_I constructed from parallelograms whose dihedral angles satisfy the uniform dihedral angle assumption will naturally inherit a flat metric. The illustration in Fig. 3(b) shows the relationship between the dihedral angle $\psi_{\{\alpha\beta\}}$ and the angle between unit normals to the cube faces, $\vec{n}_{A\{\alpha\}} = c_{\{\alpha\}} \vec{\nabla} x$ for $\alpha = \pm x$, $\vec{n}_{A\{\alpha\}} = c_{\{\alpha\}} \vec{\nabla} y$ for $\alpha = \pm y$, and $\vec{n}_{A\{\alpha\}} = c_{\{\alpha\}} \vec{\nabla} z$ for $\alpha = \pm z$. The constants $c_{\{\alpha\}}$ are chosen to ensure that the $\vec{n}_{A\{\alpha\}}$ are the outgoing unit normals. The inner products of the outgoing unit normals are related to the dihedral angles by $\vec{n}_{A\{\alpha\}} \cdot \vec{n}_{A\{\beta\}} = \cos(\pi - \psi_{A\{\alpha\beta\}}) = -\cos \psi_{A\{\alpha\beta\}}$. The inner products of the coordinate gradients also determine the coordinate components of the inverse metric: $e^{ab} = \vec{\nabla} x^a \cdot \vec{\nabla} x^b$. Therefore the flat inverse metric, $e_{A\{\alpha\beta\gamma\}}^{ab}$, associated with the vertex $A\{\alpha\beta\gamma\}$, expressed in terms of the local Cartesian coordinates of region \mathcal{B}_A , is given by

$$\begin{aligned} \partial s_{A\{\alpha\beta\gamma\}}^2 &= e_{A\{\alpha\beta\gamma\}}^{ab} \partial_a \partial_b, \\ &= \partial_x^2 + \partial_y^2 + \partial_z^2 - 2c_{\{\alpha\}}c_{\{\beta\}} \cos \psi_{A\{\alpha\beta\}} \partial_x \partial_y \\ &\quad - 2c_{\{\alpha\}}c_{\{\gamma\}} \cos \psi_{A\{\alpha\gamma\}} \partial_x \partial_z - 2c_{\{\beta\}}c_{\{\gamma\}} \cos \psi_{A\{\beta\gamma\}} \partial_y \partial_z, \end{aligned} \tag{2}$$

where the constants $c_{\{+x\}} = -c_{\{-x\}} = c_{\{+y\}} = -c_{\{-y\}} = c_{\{+z\}} = -c_{\{-z\}} = 1$ ensure the unit normals are outgoing. In Eq. (2) $\alpha = \pm x$, $\beta = \pm y$ and $\gamma = \pm z$. These metrics have the correct dihedral angles between coordinate faces to allow them to fit

Table 1

This table gives the coordinates of each of the eight cube vertices $\vec{v}_{\{\alpha\beta\gamma\}}$ with respect to the center of \mathcal{B}_A .

$\{\alpha\beta\gamma\}$	$\vec{v}_{\{\alpha\beta\gamma\}}$	$\{\alpha\beta\gamma\}$	$\vec{v}_{\{\alpha\beta\gamma\}}$
$\{-x - y - z\}$	$\frac{1}{2}L(-1, -1, -1)$	$\{-x - y + z\}$	$\frac{1}{2}L(-1, -1, +1)$
$\{-x + y - z\}$	$\frac{1}{2}L(-1, +1, -1)$	$\{-x + y + z\}$	$\frac{1}{2}L(-1, +1, +1)$
$\{+x - y - z\}$	$\frac{1}{2}L(+1, -1, -1)$	$\{+x - y + z\}$	$\frac{1}{2}L(+1, -1, +1)$
$\{+x + y - z\}$	$\frac{1}{2}L(+1, +1, -1)$	$\{+x + y + z\}$	$\frac{1}{2}L(+1, +1, +1)$

together smoothly with the metrics in neighboring regions. Since the derivatives of these metrics vanish throughout each region, they are all flat.

The final step in constructing a flat metric on the \mathcal{S}_I domain is to show that the intrinsic parts of the metrics constructed in Eq. (2) are continuous across the interface boundaries between the cubic regions in \mathcal{S}_I . Equation (2) shows that these metrics depend only on the dihedral angles of the edges of the cubic region. The simple uniform dihedral angle assumption adopted for this study implies the local reflection symmetry of the triangulations described above. This symmetry guarantees that the dihedral angles of each cubic region \mathcal{B}_A are the same as those of the neighboring cubic regions. The metrics in two neighboring regions will therefore be related to one another by the local reflection symmetry across the interface boundary between them. It follows that the intrinsic parts of the metrics must be continuous across the interface boundary. In general the gauge components of the metric will not be continuous when expressed in the Cartesian coordinates of the multicube structure.

2.3. Step 3: constructing \hat{g}_{ab}

The next step in our procedure for constructing a reference metric is to build a partition of unity that can be used to combine the flat metrics from the various overlapping domains into a global non-singular metric that is smooth within each cubic region, and whose intrinsic parts are continuous across the interfaces with each neighboring region. The needed partition of unity function $u_{A\{\alpha\beta\gamma\}}(\vec{x}) \geq 0$ has the value 1 at the $A\{\alpha\beta\gamma\}$ vertex of domain \mathcal{B}_A , and falls smoothly to zero on the faces of \mathcal{B}_A that do not intersect this vertex. The $u_{A\{\alpha\beta\gamma\}}(\vec{x})$ are positive within the star-shaped domain \mathcal{S}_I centered on the $A\{\alpha\beta\gamma\}$ vertex, and vanish on its outer boundary. They are used as weight functions to compute averages of the flat inverse metrics $e_{A\{\alpha\beta\gamma\}}^{ab}$ defined on the \mathcal{S}_I domains in Eq. (2). The inverse of the resulting average, \hat{g}_{ab} , is the global C^0 reference metric.

First introduce a set of non-negative weight functions, $w_{A\{\alpha\beta\gamma\}}(\vec{x}) \geq 0$, whose support is centered on the vertex $A\{\alpha\beta\gamma\}$. In the two-dimensional case [7] simple separable functions of the global Cartesian coordinates were used successfully for these weight functions. The three-dimensional analogs of those two-dimensional functions are

$$w_{A\{\alpha\beta\gamma\}}(\vec{x}) = h\left(\frac{\Delta x_{A\{\alpha\beta\gamma\}}}{L}\right) h\left(\frac{\Delta y_{A\{\alpha\beta\gamma\}}}{L}\right) h\left(\frac{\Delta z_{A\{\alpha\beta\gamma\}}}{L}\right), \tag{3}$$

where the index $A\{\alpha\beta\gamma\}$ refers to the vertex of the cubic region \mathcal{B}_A , and L is the coordinate size of the regions. The vectors $\vec{\Delta}x_{A\{\alpha\beta\gamma\}} = (\Delta x_{A\{\alpha\beta\gamma\}}, \Delta y_{A\{\alpha\beta\gamma\}}, \Delta z_{A\{\alpha\beta\gamma\}})$ are defined by

$$\vec{\Delta}x_{A\{\alpha\beta\gamma\}} = \vec{x} - \vec{c}_A - \vec{v}_{\{\alpha\beta\gamma\}}, \tag{4}$$

where \vec{x} are the global Cartesian coordinates of the multicube structure that are aligned with the cube faces, and where $\vec{c}_A + \vec{v}_{\{\alpha\beta\gamma\}}$ are the coordinates of the vertex $A\{\alpha\beta\gamma\}$. The values of \vec{c}_A , the locations of the centers of regions \mathcal{B}_A , are specified as part of the definition of the multicube structure; and the values of $\vec{v}_{\{\alpha\beta\gamma\}}$, the positions of the vertices relative to the centers are given in Table 1. They are the same for all the regions.

The functions $h(s)$ used in Eq. (3) are chosen to have the values $h(0) = 1$ and $h(\pm 1) = 0$. With the arguments specified in Eq. (3) this corresponds to setting $w_{A\{\alpha\beta\gamma\}} = 1$ at the vertex point $A\{\alpha\beta\gamma\}$, and $w_{A\{\alpha\beta\gamma\}} = 0$ on the boundary faces of \mathcal{B}_A that do not intersect this vertex. Each of the functions $w_{A\{\alpha\beta\gamma\}}(\vec{x})$ is also continuous across the $A\{\alpha\}$, $A\{\beta\}$, and $A\{\gamma\}$ interfaces with the corresponding functions in the neighboring domains centered on this same vertex. We find that the functions

$$h(s) = h(-s) = \frac{1}{2} \left\{ 1 + \left(1 - s^{2k}\right)^\ell - \left[1 - \left(1 - |s|^{2k}\right)^\ell\right] \right\}, \tag{5}$$

with integers $k > 0$ and $\ell > 0$, work quite well in practice. Some of these functions are illustrated in Fig. 4, with integer values in the range that worked best in our numerical tests.

The final task in constructing special partitions of unity for the region \mathcal{B}_A is to construct the normalizing functions $W_A(\vec{x})$:

$$W_A(\vec{x}) = \sum_{\{\alpha\beta\gamma\}} w_{A\{\alpha\beta\gamma\}}(\vec{x}), \tag{6}$$

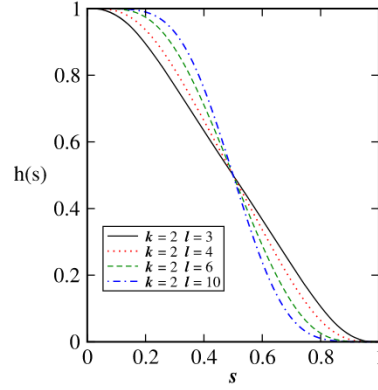


Fig. 4. Examples of the $h(s) = \frac{1}{2} \{1 + (1 - s^{2k})^\ell - [1 - (1 - |s|^{2k})^\ell]\}$ functions defined in Eq. (5) used to construct the partitions of unity for the C^0 reference metrics, and in the construction of the C^0 and C^1 reference metrics.

where $w_{A\{\alpha\beta\gamma\}}(\vec{x})$ is defined in Eq. (3). These $W_A(\vec{x})$ are strictly positive, so they can be used to define the partition of unity functions:

$$u_{A\{\alpha\beta\gamma\}}(\vec{x}) = \frac{w_{A\{\alpha\beta\gamma\}}(\vec{x})}{W_A(\vec{x})}. \quad (7)$$

This normalization ensures that these functions satisfy the inequalities $0 \leq u_{A\{\alpha\beta\gamma\}}(\vec{x}) \leq 1$, and also the usual partition of unity normalization condition

$$1 = \sum_{\{\alpha\beta\gamma\}} u_{A\{\alpha\beta\gamma\}}(\vec{x}), \quad (8)$$

for each \vec{x} in each \mathcal{B}_A .

A global reference inverse metric $\hat{g}^{ab}(\vec{x})$ for \vec{x} in region \mathcal{B}_A can now be constructed by combining the flat metrics $e_{A\{\alpha\beta\gamma\}}^{ab}$ defined in Eq. (2) with the partition of unity functions defined in that region by Eq. (7):

$$\hat{g}^{ab}(\vec{x}) = \sum_{\{\alpha\beta\gamma\}} u_{A\{\alpha\beta\gamma\}}(\vec{x}) e_{A\{\alpha\beta\gamma\}}^{ab}(\vec{x}). \quad (9)$$

The sum is over the eight vertices of region \mathcal{B}_A . This inverse metric is positive definite since it is a linear combination of positive definite inverse metrics, $e_{A\{\alpha\beta\gamma\}}^{ab}$, using the non-negative weight functions $u_{A\{\alpha\beta\gamma\}}(\vec{x})$. A global continuous reference metric, $\hat{g}_{ab}(\vec{x})$, is then obtained by inverting $\hat{g}^{ab}(\vec{x})$ at each point \vec{x} . The metric \hat{g}_{ab} has continuous intrinsic parts across all of the multicube interface boundaries because it is constructed from flat metrics and partition of unity functions that are each appropriately continuous across those interfaces.

3. Constructing a C^1 three-dimensional reference metric

In this section the C^0 metric, \hat{g}_{ab} , constructed in Sec. 2 is transformed into a C^1 metric in three steps. In the first of these steps, in Sec. 3.1, a conformal transformation is applied to \hat{g}_{ab} producing a new metric, \bar{g}_{ab} , that makes all the edges of each cubic region into geodesics while keeping the intrinsic parts of \bar{g}_{ab} continuous across the interface boundaries. This transformation also fixes one component of the associated extrinsic curvatures along the edges: $\bar{K}_{ab}^{(\alpha)} \gamma^a \gamma^b = 0$ where γ^a is tangent to the edge. (See Sec. 3.2 for details.) In the second step, in Sec. 3.2, the metric \bar{g}_{ab} is transformed to produce a new metric, $\bar{\bar{g}}_{ab}$, whose intrinsic components on each cube face are identical to those of \bar{g}_{ab} , but whose extrinsic curvatures, $\bar{\bar{K}}_{ab}^{(\alpha)}$, vanish identically on each edge of each cubic region. In the third step, in Sec. 3.3, the metric $\bar{\bar{g}}_{ab}$ is adjusted in the interiors of each cubic region (keeping its boundary values fixed) in such a way that the resulting metric \tilde{g}_{ab} has extrinsic curvatures $\tilde{K}_{ab}^{(\alpha)}$ that vanish identically on each cube face. The \tilde{g}_{ab} metric constructed by these three steps preserves the continuity of the intrinsic components of the metric \hat{g}_{ab} across each interface boundary. This intrinsic metric continuity together with the continuity of the extrinsic curvatures across the interface boundaries (which vanish identically on those boundaries in this case) are the geometric Israel junction conditions [8] needed to ensure that the metric \tilde{g}_{ab} is C^1 across those interfaces.

The methods used in this section are quite general. In particular, they do not depend on the uniform dihedral angle assumption used in Sec. 2 to construct \hat{g}_{ab} . The only specialized assumption used here, specifically in Sec. 3.2, requires that the dihedral angles are constants along each cube edge. This additional assumption is satisfied automatically by the \hat{g}_{ab} metrics constructed in Sec. 2 using the uniform dihedral angle assumption, but it will not be satisfied in the most

general case. All that is required to avoid conical singularities is the sum of the dihedral angles (from each of the cubes that intersect at an edge) equal 2π at each point along the edge. So the dihedral angle in any one cube may (and perhaps will) in the general case vary along an edge, so long as the global sum constraint is satisfied. In this general case, the construction of the C^1 metrics described here, particularly the parts described in Sec. 3.2, will have to be generalized as well.

3.1. Step 1: converting \hat{g}_{ab} into \bar{g}_{ab}

This section constructs a conformal factor, e^ϕ , that is used to transform the reference metric \hat{g}_{ab} constructed in Sec. 2.3:

$$\bar{g}_{ab} = e^\phi \hat{g}_{ab}. \quad (10)$$

The geodesic equation for the curve $x^a(s)$ in the \bar{g}_{ab} metric is given by

$$\frac{d^2 x^a}{ds^2} + \bar{\Gamma}_{bc}^a \frac{dx^b}{ds} \frac{dx^c}{ds} = A(s) \frac{dx^a}{ds}, \quad (11)$$

where s is an arbitrary parameterization of this curve, where $\bar{\Gamma}_{bc}^a$ are the Christoffel symbols of the second kind for this metric, and where $A(s)$ is a parameter dependent function. The idea is to choose a conformal factor e^ϕ in Eq. (10) having two properties: *a*) it makes each edge of each cubic region into a geodesic of the metric \bar{g}_{ab} , and *b*) it is continuous across each cube interface.

Consider the cubic region, \mathcal{B}_A , whose Cartesian coordinates are labeled $x^a = \{x^\alpha, x^\beta, x^\gamma\}$, and consider the $A\{\alpha\beta\}$ edge of this region where the $A\{\alpha\}$ and $A\{\beta\}$ faces intersect. This edge is a curve with tangent vector $dx^a/ds = \{0, 0, 1\}$, where the parameter s has been chosen to be $s = x^\gamma$. An equivalent form of this equation, more convenient for these purposes, is given by

$$\bar{g}_{ab} \frac{d^2 x^b}{ds^2} + \bar{\Gamma}_{abc} \frac{dx^b}{ds} \frac{dx^c}{ds} = A(s) \bar{g}_{ab} \frac{dx^b}{ds}, \quad (12)$$

where the $\bar{\Gamma}_{abc}$ are the Christoffel symbols of the first kind. The three components of this equation can be reduced to

$$\partial_\gamma \bar{g}_{\alpha\gamma} - \frac{1}{2} \partial_\alpha \bar{g}_{\gamma\gamma} = A(s) \bar{g}_{\alpha\gamma}, \quad (13)$$

$$\partial_\gamma \bar{g}_{\beta\gamma} - \frac{1}{2} \partial_\beta \bar{g}_{\gamma\gamma} = A(s) \bar{g}_{\beta\gamma}, \quad (14)$$

$$\frac{1}{2} \partial_\gamma \bar{g}_{\gamma\gamma} = A(s) \bar{g}_{\gamma\gamma}. \quad (15)$$

As an interesting aside, note that Eq. (13) depends only on the intrinsic metric on face $A\{\beta\}$, and together with Eq. (15) forms the intrinsic geodesic equation on this face. Similarly Eq. (14) depends only on the intrinsic metric on face $A\{\alpha\}$, and together with Eq. (15) forms the intrinsic geodesic equation on this face. Thus the curve formed by the intersection of two surfaces is a geodesic of the full three-dimensional space if and only if it is a geodesic of the intrinsic geometry of each surface separately.

The idea now is to choose a conformal factor ϕ that transforms \hat{g}_{ab} , using Eq. (10), so the resulting \bar{g}_{ab} satisfies Eqs. (13)–(15) on the edges of each cubic region. The intrinsic parts of the resulting \bar{g}_{ab} will be continuous across the interfaces between regions if and only if the conformal factor ϕ is continuous across those interfaces. First set $\phi = 0$ along the edges of the cubic region to ensure that \bar{g}_{ab} is continuous there. In this case Eqs. (13)–(15) can be re-written in terms of \hat{g}_{ab} and ϕ for points along the $A\{\alpha\beta\}$ edge:

$$\partial_\gamma \hat{g}_{\alpha\gamma} - \frac{1}{2} \partial_\alpha \hat{g}_{\gamma\gamma} - \frac{1}{2} \hat{g}_{\gamma\gamma} \partial_\alpha \phi = A(s) \hat{g}_{\alpha\gamma}, \quad (16)$$

$$\partial_\gamma \hat{g}_{\beta\gamma} - \frac{1}{2} \partial_\beta \hat{g}_{\gamma\gamma} - \frac{1}{2} \hat{g}_{\gamma\gamma} \partial_\beta \phi = A(s) \hat{g}_{\beta\gamma}, \quad (17)$$

$$\frac{1}{2} \partial_\gamma \hat{g}_{\gamma\gamma} = A(s) \hat{g}_{\gamma\gamma}. \quad (18)$$

The terms involving $\partial_\gamma \phi$ all vanish in these equations because $\phi = 0$ along this edge. These equations place constraints on $\partial_\alpha \phi$ and $\partial_\beta \phi$. In particular, Eq. (18), determines $A(s)$ in terms of $\hat{g}_{\gamma\gamma}$, while Eqs. (16) and (17), can be re-written as boundary conditions for $\partial_a \phi$ along the $A\{\alpha\beta\}$ edge:

$$\partial_\alpha \phi_{\{A\alpha\beta\}} = \frac{2 \partial_\gamma \hat{g}_{\alpha\gamma} - \partial_\alpha \hat{g}_{\gamma\gamma}}{\hat{g}_{\gamma\gamma}} - \frac{\hat{g}_{\alpha\gamma} \partial_\gamma \hat{g}_{\gamma\gamma}}{(\hat{g}_{\gamma\gamma})^2}, \quad (19)$$

$$\partial_\beta \phi_{\{A\alpha\beta\}} = \frac{2 \partial_\gamma \hat{g}_{\beta\gamma} - \partial_\beta \hat{g}_{\gamma\gamma}}{\hat{g}_{\gamma\gamma}} - \frac{\hat{g}_{\beta\gamma} \partial_\gamma \hat{g}_{\gamma\gamma}}{(\hat{g}_{\gamma\gamma})^2}. \quad (20)$$

Note that these expressions imply that the conformal factor ϕ will not vanish everywhere on the cube faces unless $0 = \hat{\Gamma}_{\alpha\gamma\gamma}$ on the edges, in which case those edges would already be geodesics of the \hat{g}_{ab} metric. Also note that the metric \hat{g}_{ab} constructed in Sec. 2 rapidly approaches a constant flat metric at each vertex of the cubic region. It follows that the connection $\hat{\Gamma}_{abc}$ and the gradient $\partial_a\phi$ all vanish at these vertex points.

The next step is to extend the conformal factor ϕ across the faces of the cubic region \mathcal{B}_A in a way that a) satisfies the boundary conditions given in Eqs. (19) and (20) along each edge, and b) ensures that it is continuous across the interface with the neighboring cubic region. The conformal factor $\phi_{A\{\alpha\}}$ on the $A\{\alpha\}$ face satisfies the boundary conditions $\phi_{A\{\alpha\beta\}} = 0$ and Eq. (20) along the $A\{\alpha\beta\}$ edge. Analogous conditions must also be imposed on each edge of this face. Together, these conditions constitute Dirichlet and Neumann boundary conditions for $\phi_{A\{\alpha\}}$ on the $A\{\alpha\}$ face. One convenient way to find $\phi_{A\{\alpha\}}$ that satisfy these boundary conditions is to solve the bi-harmonic equation for $\phi_{A\{\alpha\}}$ on this face:

$$\left(\partial_\beta^4 + 2\partial_\beta^2\partial_\gamma^2 + \partial_\gamma^4\right)\phi_{A\{\alpha\}} = 0. \quad (21)$$

Solutions to the bi-harmonic equation are uniquely determined by specifying both Dirichlet and Neumann conditions on the boundary of a compact domain [16]. This approach can then be used to determine the surface values of ϕ on each face of each region in the multicube structure. The pseudo-spectral numerical methods used to solve this equation for this study are described briefly in Appendix B.

The boundary conditions that determine the solution to Eq. (21) only depend on the intrinsic components of the metric, $\hat{g}_{\beta\beta}$, $\hat{g}_{\beta\gamma}$ and $\hat{g}_{\gamma\gamma}$, on the $A\{\alpha\}$ face. These intrinsic metric components were constructed to be continuous across this interface boundary in Sec. 2. It follows that boundary conditions used to determine $\phi_{A\{\alpha\}}$ will be the same on both sides of the interface boundary. Since the solution to Eq. (21) with Dirichlet and Neumann boundary conditions is unique [16], it follows that the $\phi_{A\{\alpha\}}$ determined in this way will be the same on both sides of the interface.

The method described above can be used to determine the surface values $\phi_{A\{\alpha\}}$ on each face of each cubic region. These solutions provide Dirichlet boundary conditions for the full conformal factor ϕ_A within each region. The normal derivatives of $\phi_{A\{\alpha\}}$ are unconstrained, however, beyond the requirement that those derivatives agree along the edges with the tangential derivatives from the neighboring faces. The conformal factor ϕ within the cubic region can therefore be determined in any number of ways. For example, it could be determined by solving the three-dimensional Laplace equation with the Dirichlet boundary conditions $\phi_{A\{\alpha\}}$.

A computationally more efficient approach has been adopted for this study. Begin by defining a set of coordinates s_A^α that measure the relative distance between a point inside region \mathcal{B}_A and the $\partial_{-\alpha}\mathcal{B}_A$ face of that region. The s_A^α are normalized so that $s_A^\alpha = 0$ on the $\partial_\alpha\mathcal{B}_A$ face, while $s_A^\alpha = 1$ on the opposite $\partial_{-\alpha}\mathcal{B}_A$ face. In particular

$$s_A^{\pm x} = \left| \frac{x - c_A^x}{L} \mp \frac{1}{2} \right|, \quad s_A^{\pm y} = \left| \frac{y - c_A^y}{L} \mp \frac{1}{2} \right|, \quad s_A^{\pm z} = \left| \frac{z - c_A^z}{L} \mp \frac{1}{2} \right|, \quad (22)$$

where $\bar{x} = (x, y, z)$ are the global Cartesian coordinates of the multicube structure, $\bar{c}_A = (c_A^x, c_A^y, c_A^z)$ are the coordinates of the center, and L is the coordinate size of region \mathcal{B}_A .

The conformal factor $\phi_{A\{\alpha\}}$ on the $A\{\alpha\}$ face, constructed by solving Eq. (21), can now be extrapolated into the interior using the $h(s)$ functions defined in Eq. (5). Consider the extrapolation $\phi_A^\alpha = h(s_A^\alpha)\phi_{A\{\alpha\}}$. The $\phi_{A\{\alpha\}}$ vanish identically along the edges because of the boundary conditions used to solve Eq. (21). Therefore the $\phi_{A\{\alpha\}}$ extrapolated in this way do not modify the $\phi_{A\{\beta\}}$ on the adjacent faces. It does not modify $\phi_{A\{-\alpha\}}$ on the opposite face, either, because $h(s_A^\alpha)$ vanishes there. The complete conformal factor ϕ_A in the interior of region \mathcal{B}_A can therefore be determined by combining the extrapolations from all the cube faces:

$$\phi_A = \sum_\alpha \phi_A^\alpha = \sum_\alpha h(s_A^\alpha)\phi_{A\{\alpha\}}. \quad (23)$$

The resulting ϕ_A automatically satisfies the Dirichlet conditions $\phi_{A\{\alpha\}}$ on each of the faces.

The conditions in Eqs. (19) and (20) ensure that the edges of each cubic region are geodesics of the metric $\bar{g}_{ab} = e^\phi\hat{g}_{ab}$. The continuity across the interface boundaries of ϕ_A ensures that the global solution for ϕ is continuous across those boundaries. And this in turn ensures that the intrinsic components of the \bar{g}_{ab} metric are continuous across all the interface boundaries as well.

3.2. Step 2: converting \bar{g}_{ab} into $\bar{\bar{g}}_{ab}$

Let \bar{g}_{ab} denote the global C^0 metric constructed in Sec. 3.1. The goal of this second step is to convert \bar{g}_{ab} into a metric $\bar{\bar{g}}_{ab}$ having two important properties: first, the extrinsic curvatures $\bar{K}_{ab}^{(\alpha)}$ associated with $\bar{\bar{g}}_{ab}$ must vanish identically on each edge of each cubic region; and second, the intrinsic parts of $\bar{\bar{g}}_{ab}$ must be identical to those of \bar{g}_{ab} . We note that while \bar{g}_{ab} was constructed to have intrinsic parts that are only C^0 across the interface boundaries, within each region \bar{g}_{ab} is actually smooth.

Consider the interface boundary $A\{\alpha\}$ of cubic region \mathcal{B}_A . In the global Cartesian coordinates of our multicube structure, the boundary $A\{\alpha\}$ is a level surface of the coordinate x^α . The unit normal co-vector field to the foliation of constant x^α surfaces, $\bar{n}_a^{(\alpha)}$, is given by

$$\bar{n}_a^{(\alpha)} = \bar{N}^{(\alpha)} \partial_a x^\alpha, \quad (24)$$

where $\bar{N}^{(\alpha)} = \epsilon^{(\alpha)} (\bar{g}^{\alpha\alpha})^{-1/2}$. The constant $\epsilon^{(\alpha)} = \pm 1$ determines the sign of $\bar{N}^{(\alpha)}$, and is chosen to ensure that $\bar{n}_a^{(\alpha)}$ is the outward directed unit normal on the $A\{\alpha\}$ face. The extrinsic curvature $\bar{K}_{ab}^{(\alpha)}$ of this surface is given by

$$\bar{K}_{ab}^{(\alpha)} = \bar{P}_a^{(\alpha)c} \bar{P}_b^{(\alpha)d} \bar{\nabla}_c \bar{n}_d^{(\alpha)} \quad (25)$$

$$= \bar{P}_a^{(\alpha)c} \bar{P}_b^{(\alpha)d} \left(\partial_c \bar{n}_d^{(\alpha)} - \bar{n}_e^{(\alpha)} \bar{\Gamma}_{cd}^e \right) \quad (26)$$

$$= \frac{1}{2} \bar{P}_a^{(\alpha)c} \bar{P}_b^{(\alpha)d} \bar{n}^{(\alpha)e} \left(\partial_e \bar{g}_{cd} - \partial_c \bar{g}_{ed} - \partial_d \bar{g}_{ec} \right), \quad (27)$$

where $\bar{\nabla}_c$ is the \bar{g}_{ab} metric-compatible covariant derivative, and $\bar{P}_a^{(\alpha)c}$ is the projection tensor $\bar{P}_a^{(\alpha)c} = \delta_a^c - \bar{n}_a^{(\alpha)} \bar{n}^{(\alpha)c}$. Note that the term proportional to $\partial_c \bar{n}_d^{(\alpha)} = \partial_c \bar{N}^{(\alpha)} \partial_d x^\alpha$ in Eq. (26) vanishes identically because $\bar{P}_b^{(\alpha)d} \partial_d x^\alpha = 0$.

We define the difference between the \bar{g}_{ab} and the \bar{g}_{ab} metrics, $\delta \bar{g}_{ab}$, and the associated differences between extrinsic curvatures, $\delta \bar{K}_{ab}^{(\alpha)}$:

$$\delta \bar{g}_{ab} = \bar{g}_{ab} - \bar{g}_{ab}, \quad (28)$$

$$\delta \bar{K}_{ab}^{(\alpha)} = \bar{K}_{ab}^{(\alpha)} - \bar{K}_{ab}^{(\alpha)}. \quad (29)$$

Note that these differences are not necessarily infinitesimal. To ensure that the intrinsic parts of \bar{g}_{ab} are identical to those of \bar{g}_{ab} , we choose $\delta \bar{g}_{ab}$ to be a smooth tensor in the interior of each cubic region that satisfies,

$$\bar{P}_a^{(\alpha)c} \bar{P}_b^{(\alpha)d} \delta \bar{g}_{cd} = 0 \quad (30)$$

on each cube face $A\{\alpha\}$. Note that the projection tensor $\bar{P}_a^{(\alpha)c}$ is identical to $\bar{P}_a^{(\alpha)c}$ on $A\{\alpha\}$ because $\bar{P}_a^{(\alpha)c} \partial_c x^\alpha = \bar{P}_a^{(\alpha)c} \partial_c x^\alpha = 0$. Therefore the metric continuity condition on $\delta \bar{g}_{ab}$ is equivalent to

$$\bar{P}_a^{(\alpha)c} \bar{P}_b^{(\alpha)d} \delta \bar{g}_{cd} = 0, \quad (31)$$

which is easier to enforce since the metric \bar{g}_{ab} , and consequently the normal vector $\bar{n}_a^{(\alpha)}$, is already known. The condition that the extrinsic curvature $\bar{K}_{ab}^{(\alpha)}$ vanishes along each edge of the $A\{\alpha\}$ face can be expressed as the following condition on $\delta \bar{K}_{ab}^{(\alpha)}$,

$$\delta \bar{K}_{ab}^{(\alpha)} = -\bar{K}_{ab}^{(\alpha)}, \quad (32)$$

on each edge of each cube face $A\{\alpha\}$.

To determine exactly what restrictions are placed on $\delta \bar{g}_{ab}$ by the intrinsic metric and extrinsic curvature continuity conditions, Eqs. (31)–(32), we examine those conditions expressed in the Cartesian coordinates $\{x^\alpha, x^\beta, x^\gamma\}$ of region \mathcal{B}_A . The $A\{\alpha\}$ face of this region is defined by an $x^\alpha = \text{constant}$ surface, while the x^β and x^γ coordinates label points on that face. In these coordinates the intrinsic metric continuity condition, Eq. (31), implies that all the x^β and x^γ components of the metric perturbation vanish everywhere on that face: $\delta \bar{g}_{\beta\beta} = \delta \bar{g}_{\beta\gamma} = \delta \bar{g}_{\gamma\gamma} = 0$. Similarly on the adjacent $A\{\beta\}$ face, all the x^α and x^γ components of the metric perturbation vanish $\delta \bar{g}_{\alpha\alpha} = \delta \bar{g}_{\alpha\gamma} = \delta \bar{g}_{\gamma\gamma} = 0$. It follows that all the components of $\delta \bar{g}_{ab}$ except $\delta \bar{g}_{\alpha\beta}$ must vanish along the $A\{\alpha\beta\}$ edge: $\delta \bar{g}_{\alpha\alpha} = \delta \bar{g}_{\alpha\gamma} = \delta \bar{g}_{\beta\beta} = \delta \bar{g}_{\beta\gamma} = \delta \bar{g}_{\gamma\gamma} = 0$.

The C^0 metric \bar{g}_{ab} was constructed so that the dihedral angle between the $A\{\alpha\}$ and $A\{\beta\}$ faces, $\cos \psi_{\{A\alpha\beta\}} = -\bar{g}^{\alpha\beta} / \sqrt{\bar{g}^{\alpha\alpha} \bar{g}^{\beta\beta}}$, is constant along the edge between these faces. This was done to ensure there is no conical singularity along this edge. To ensure that the \bar{g}_{ab} metric has no conical singularity there, we keep this dihedral angle fixed in this metric along this edge as well. This can be done by imposing the additional constraint $\delta \bar{g}_{\alpha\beta} = 0$ along this edge. This makes all the components $\delta \bar{g}_{ab} = 0$, and consequently $\delta \bar{g}^{ab} = 0$ which keeps the dihedral angles fixed. Thus the intrinsic metric continuity conditions, along with the conditions to ensure there are no conical singularities along the edges, require that all the components of the metric perturbation vanish along each edge: $\delta \bar{g}_{ab} = 0$.

Exact expressions for the x^β and x^γ components of the extrinsic curvature $\bar{K}_{ab}^{(\alpha)}$ on the $A\{\alpha\}$ face are obtained from Eqs. (27) and (28):

$$\bar{K}_{\beta\beta}^{(\alpha)} = \frac{1}{2} \bar{n}^{(\alpha)a} \left(\partial_a \bar{g}_{\beta\beta} - 2\partial_\beta \bar{g}_{a\beta} \right) + \frac{1}{2} \bar{n}^{(\alpha)a} \left(\partial_a \delta \bar{g}_{\beta\beta} - 2\partial_\beta \delta \bar{g}_{a\beta} \right), \quad (33)$$

$$\bar{K}_{\beta\gamma}^{(\alpha)} = \frac{1}{2} \bar{n}^{(\alpha)a} \left(\partial_a \bar{g}_{\beta\gamma} - \partial_\beta \bar{g}_{a\gamma} - \partial_\gamma \bar{g}_{a\beta} \right) + \frac{1}{2} \bar{n}^{(\alpha)a} \left(\partial_a \delta \bar{g}_{\beta\gamma} - \partial_\beta \delta \bar{g}_{a\gamma} - \partial_\gamma \delta \bar{g}_{a\beta} \right), \quad (34)$$

$$\bar{K}_{\gamma\gamma}^{(\alpha)} = \frac{1}{2} \bar{n}^{(\alpha)a} \left(\partial_a \bar{g}_{\gamma\gamma} - 2\partial_\gamma \bar{g}_{a\gamma} \right) + \frac{1}{2} \bar{n}^{(\alpha)a} \left(\partial_a \delta \bar{g}_{\gamma\gamma} - 2\partial_\gamma \delta \bar{g}_{a\gamma} \right). \quad (35)$$

On the $A\{\alpha\beta\}$ edge, where the $A\{\alpha\}$ and $A\{\beta\}$ faces intersect, $\delta\bar{g}_{ab} = 0$, so $\bar{n}^{(\alpha)a} = \bar{n}^{(\alpha)a}$. Consequently Eqs. (33)–(35) can be re-written in the simpler form:

$$\delta\bar{K}_{\beta\beta}^{(\alpha)} = \bar{K}_{\beta\beta}^{(\alpha)} - \bar{K}_{\beta\beta}^{(\alpha)} = \frac{1}{2}\bar{n}^{(\alpha)a} (\partial_a \delta\bar{g}_{\beta\beta} - 2\partial_\beta \delta\bar{g}_{a\beta}), \quad (36)$$

$$\delta\bar{K}_{\beta\gamma}^{(\alpha)} = \bar{K}_{\beta\gamma}^{(\alpha)} - \bar{K}_{\beta\gamma}^{(\alpha)} = \frac{1}{2}\bar{n}^{(\alpha)a} (\partial_a \delta\bar{g}_{\beta\gamma} - \partial_\beta \delta\bar{g}_{a\gamma} - \partial_\gamma \delta\bar{g}_{a\beta}), \quad (37)$$

$$\delta\bar{K}_{\gamma\gamma}^{(\alpha)} = \bar{K}_{\gamma\gamma}^{(\alpha)} - \bar{K}_{\gamma\gamma}^{(\alpha)} = \frac{1}{2}\bar{n}^{(\alpha)a} (\partial_a \delta\bar{g}_{\gamma\gamma} - 2\partial_\gamma \delta\bar{g}_{a\gamma}). \quad (38)$$

Since $\delta\bar{g}_{ab} = 0$ along the $A\{\alpha\beta\}$ edge, it follows that $\partial_\gamma \delta\bar{g}_{ab} = 0$ there. Since $\delta\bar{g}_{\beta\beta} = \delta\bar{g}_{\beta\gamma} = \delta\bar{g}_{\gamma\gamma} = 0$ everywhere on the $A\{\alpha\}$ face, it follows that $\partial_\beta \delta\bar{g}_{\beta\beta} = \partial_\beta \delta\bar{g}_{\beta\gamma} = \partial_\beta \delta\bar{g}_{\gamma\gamma} = 0$ along the $A\{\alpha\beta\}$ edge as well. Finally, $\delta\bar{g}_{\gamma\gamma}$ on the adjacent $\partial_\beta \mathcal{B}_A$ face represents a perturbation of the intrinsic metric, so $\partial_\alpha \delta\bar{g}_{\gamma\gamma} = 0$ along the $A\{\alpha\beta\}$ edge as well. The components of $\bar{n}^{(\alpha)a}$ in these coordinates are given by $\bar{n}^{(\alpha)a} = \bar{N}^{(\alpha)} \{\bar{g}^{\alpha\alpha}, \bar{g}^{\alpha\beta}, \bar{g}^{\alpha\gamma}\}$, so the expressions for $\delta\bar{K}_{ab}^{(\alpha)}$ from Eqs. (36)–(38) can be simplified further:

$$\delta\bar{K}_{\beta\beta}^{(\alpha)} = \frac{1}{2}\bar{N}^{(\alpha)} \bar{g}^{\alpha\alpha} (\partial_\alpha \delta\bar{g}_{\beta\beta} - 2\partial_\beta \delta\bar{g}_{\alpha\beta}), \quad (39)$$

$$\delta\bar{K}_{\beta\gamma}^{(\alpha)} = \frac{1}{2}\bar{N}^{(\alpha)} \bar{g}^{\alpha\alpha} (\partial_\alpha \delta\bar{g}_{\beta\gamma} - \partial_\beta \delta\bar{g}_{\alpha\gamma}), \quad (40)$$

$$\delta\bar{K}_{\gamma\gamma}^{(\alpha)} = 0. \quad (41)$$

The analogous expressions for $\delta\bar{K}_{ab}^{(\beta)}$, the extrinsic curvature of the adjacent $A\{\beta\}$ face, along this edge can be obtained by interchanging the roles of x^α and x^β in Eqs. (39)–(41):

$$\delta\bar{K}_{\alpha\alpha}^{(\beta)} = \frac{1}{2}\bar{N}^{(\beta)} \bar{g}^{\beta\beta} (\partial_\beta \delta\bar{g}_{\alpha\alpha} - 2\partial_\alpha \delta\bar{g}_{\alpha\beta}), \quad (42)$$

$$\delta\bar{K}_{\alpha\gamma}^{(\beta)} = \frac{1}{2}\bar{N}^{(\beta)} \bar{g}^{\beta\beta} (\partial_\beta \delta\bar{g}_{\alpha\gamma} - \partial_\alpha \delta\bar{g}_{\beta\gamma}), \quad (43)$$

$$\delta\bar{K}_{\gamma\gamma}^{(\beta)} = 0. \quad (44)$$

These expressions for $\delta\bar{K}_{\beta\beta}^{(\alpha)}$ and $\delta\bar{K}_{\alpha\gamma}^{(\beta)}$ define the required boundary conditions on the derivatives $\partial_a \delta\bar{g}_{ab}$ along the $A\{\alpha\beta\}$ edge, where the $A\{\alpha\}$ and $A\{\beta\}$ faces intersect. Since $\delta\bar{K}_{ab}^{(\alpha)}$ must satisfy Eq. (32), we see that these boundary conditions imply that the gauge components of the metric (i.e. the non-intrinsic components) $\delta\bar{g}_{\alpha\alpha}$, $\delta\bar{g}_{\alpha\beta}$, and $\delta\bar{g}_{\alpha\gamma}$ cannot simply be set to zero on the $A\{\alpha\}$ face.

The expressions for $\delta\bar{K}_{\beta\beta}^{(\alpha)}$ and $\delta\bar{K}_{\alpha\gamma}^{(\beta)}$, Eqs. (41) and (44), along the $A\{\alpha\beta\}$ edge, imply that no discontinuity in $\bar{K}_{\beta\beta}^{(\alpha)}$ or $\bar{K}_{\alpha\gamma}^{(\beta)}$ along this edge can be removed by any $\delta\bar{g}_{ab}$ allowed by our constraints. To understand what that means, let γ^a be the components of the vector $\partial_\gamma = \gamma^a \partial_a$. This vector is orthogonal to the surface normals: $0 = \bar{n}_a^{(\alpha)} \gamma^a = \bar{n}_a^{(\beta)} \gamma^a$. It follows that $\bar{K}_{\beta\beta}^{(\alpha)} = \gamma^a \gamma^b \bar{\nabla}_a \bar{n}_b^{(\alpha)} = \gamma^a \bar{\nabla}_a (\bar{n}_b^{(\alpha)} \gamma^b) - \bar{n}_b^{(\alpha)} \gamma^a \bar{\nabla}_a \gamma^b = -\bar{n}_b^{(\alpha)} \gamma^a \bar{\nabla}_a \gamma^b$. Since the metric \bar{g}_{ab} constructed in Sec. 3.1 has the property that each edge is a geodesic, $\gamma^a \bar{\nabla}_a \gamma^b = A(x^\gamma) \gamma^b$ (for some function $A(x^\gamma)$ along this edge), it follows that $\bar{K}_{\beta\beta}^{(\alpha)} = 0$ and similarly $\bar{K}_{\alpha\gamma}^{(\beta)} = 0$ along the $A\{\alpha\beta\}$ edge. This component of the extrinsic curvature continuity condition Eq. (32) is therefore satisfied automatically along this edge, so $\delta\bar{K}_{\beta\beta}^{(\alpha)} = \delta\bar{K}_{\alpha\gamma}^{(\beta)} = 0$ are the appropriate corrections there.

The right sides of Eqs. (40) and (43) are both proportional to $\partial_\beta \delta\bar{g}_{\alpha\gamma} - \partial_\alpha \delta\bar{g}_{\beta\gamma}$, so the extrinsic curvature perturbations on the left sides must also be related: $\bar{N}^{(\beta)} \delta\bar{K}_{\alpha\gamma}^{(\beta)} = -\bar{N}^{(\alpha)} \delta\bar{K}_{\beta\gamma}^{(\alpha)}$, obtained by simplifying using $\bar{N}^{(\alpha)} = \epsilon^{(\alpha)} (\bar{g}^{\alpha\alpha})^{-1/2}$ and $\bar{N}^{(\beta)} = \epsilon^{(\beta)} (\bar{g}^{\beta\beta})^{-1/2}$. This condition is inconsistent with Eq. (32) unless

$$\bar{N}^{(\beta)} \bar{K}_{\alpha\gamma}^{(\beta)} = -\bar{N}^{(\alpha)} \bar{K}_{\beta\gamma}^{(\alpha)}. \quad (45)$$

The simple proof of this identity is given in Appendix C. This identity shows that the edge constraints given in Eqs. (40) and (43) for $\delta\bar{K}_{\beta\gamma}^{(\alpha)}$ and $\delta\bar{K}_{\alpha\gamma}^{(\beta)}$ are self-consistent.

Equation (32) together with Eqs. (39)–(44) place the following constraints on the derivatives of certain components of $\delta\bar{g}_{ab}$ along the $A\{\alpha\beta\}$ edge,

$$\partial_\alpha \delta\bar{g}_{\beta\beta} - 2\partial_\beta \delta\bar{g}_{\alpha\beta} = -2\bar{N}^{(\alpha)} \bar{K}_{\beta\beta}^{(\alpha)}, \quad (46)$$

$$\partial_\alpha \delta\bar{g}_{\beta\gamma} - \partial_\beta \delta\bar{g}_{\alpha\gamma} = -2\bar{N}^{(\alpha)} \bar{K}_{\beta\gamma}^{(\alpha)} = 2\bar{N}^{(\beta)} \bar{K}_{\alpha\gamma}^{(\beta)}, \quad (47)$$

$$\partial_\beta \delta\bar{g}_{\alpha\alpha} - 2\partial_\alpha \delta\bar{g}_{\alpha\beta} = -2\bar{N}^{(\beta)} \bar{K}_{\alpha\alpha}^{(\beta)}. \quad (48)$$

The metric perturbation components $\delta\bar{g}_{\alpha\alpha}$, $\delta\bar{g}_{\alpha\beta}$, and $\delta\bar{g}_{\alpha\gamma}$ do not affect the intrinsic metric on the $A\{\alpha\}$ face, while the $\delta\bar{g}_{\beta\beta}$, $\delta\bar{g}_{\beta\alpha}$ and $\delta\bar{g}_{\beta\gamma}$ components do not affect the intrinsic metric on the $A\{\beta\}$ face. These components therefore play the

role of gauge degrees of freedom on these faces, which can be chosen arbitrarily subject to the constraints in Eqs. (46)–(48). While not unique, one self-consistent way to satisfy these constraints along the $A\{\alpha\beta\}$ edge is given by

$$\partial_\beta \delta \bar{g}_{\alpha\alpha} = -2\bar{N}^{(\beta)} \bar{K}_{\alpha\alpha}^{(\beta)}, \quad (49)$$

$$\partial_\beta \delta \bar{g}_{\alpha\beta} = 0, \quad (50)$$

$$\partial_\beta \delta \bar{g}_{\alpha\gamma} = -\bar{N}^{(\beta)} \bar{K}_{\alpha\gamma}^{(\beta)}, \quad (51)$$

$$\partial_\alpha \delta \bar{g}_{\beta\beta} = -2\bar{N}^{(\alpha)} \bar{K}_{\beta\beta}^{(\alpha)}, \quad (52)$$

$$\partial_\alpha \delta \bar{g}_{\beta\alpha} = 0, \quad (53)$$

$$\partial_\alpha \delta \bar{g}_{\beta\gamma} = -\bar{N}^{(\alpha)} \bar{K}_{\beta\gamma}^{(\alpha)}. \quad (54)$$

We note that the equations for $\delta \bar{g}_{\beta\beta}$, $\delta \bar{g}_{\beta\alpha}$, and $\delta \bar{g}_{\beta\gamma}$ in Eqs. (52)–(54) can be obtained from those for $\delta \bar{g}_{\alpha\alpha}$, $\delta \bar{g}_{\alpha\beta}$, and $\delta \bar{g}_{\alpha\gamma}$ in Eqs. (49)–(51) simply by exchanging the α and β indices.

The intrinsic components of the metric perturbations $\delta \bar{g}_{ab}$ must vanish on the $A\{\alpha\}$ face, $0 = \delta \bar{g}_{\beta\beta} = \delta \bar{g}_{\beta\gamma} = \delta \bar{g}_{\gamma\gamma}$. It follows from Eqs. (49)–(51) that the full set of boundary conditions on $\delta \bar{g}_{ab}$ along the $A\{\alpha\beta\}$ edge of the $A\{\alpha\}$ face are given by

$$\delta \bar{g}_{ab} = 0, \quad (55)$$

$$\partial_\beta \delta \bar{g}_{\alpha\alpha} = -2\bar{N}^{(\beta)} \bar{K}_{\alpha\alpha}^{(\beta)}, \quad (56)$$

$$\partial_\beta \delta \bar{g}_{\alpha\gamma} = -\bar{N}^{(\beta)} \bar{K}_{\alpha\gamma}^{(\beta)}, \quad (57)$$

$$\partial_\beta \delta \bar{g}_{\alpha\beta} = \partial_\beta \delta \bar{g}_{\beta\beta} = \partial_\beta \delta \bar{g}_{\beta\gamma} = \partial_\beta \delta \bar{g}_{\gamma\gamma} = 0. \quad (58)$$

When the analogs of the conditions in Eqs. (55)–(58) are enforced along all four edges of the $A\{\alpha\}$ face, they constitute both Dirichlet and Neumann conditions for the metric perturbations, $\delta \bar{g}_{ab}^{(\alpha)}$, on this face. One convenient way to find $\delta \bar{g}_{ab}^{(\alpha)}$ that satisfy these boundary conditions is to solve the bi-harmonic equation on this face:

$$\left(\partial_\beta^4 + 2 \partial_\beta^2 \partial_\gamma^2 + \partial_\gamma^4 \right) \delta \bar{g}_{ab}^{(\alpha)} = 0. \quad (59)$$

Solutions to the bi-harmonic equation are uniquely determined by specifying both Dirichlet and Neumann boundary conditions on the boundary of a compact domain. For the intrinsic components on this face, the solutions with these boundary conditions are trivial: $0 = \delta \bar{g}_{\beta\beta}^{(\alpha)} = \delta \bar{g}_{\beta\gamma}^{(\alpha)} = \delta \bar{g}_{\gamma\gamma}^{(\alpha)}$. For the non-trivial gauge components, $\delta \bar{g}_{\alpha\alpha}^{(\alpha)}$, $\delta \bar{g}_{\alpha\beta}^{(\alpha)}$, and $\delta \bar{g}_{\alpha\gamma}^{(\alpha)}$, we use pseudo-spectral methods to solve this equation numerically, as described in Appendix B. We repeat this procedure to determine $\delta \bar{g}_{ab}$ satisfying all the edge boundary conditions on all the faces of each cubic region.

The solutions to Eq. (59) determine Dirichlet boundary conditions for $\delta \bar{g}_{ab}$ on all the faces of cubic region \mathcal{B}_A . The normal derivatives of $\delta \bar{g}_{ab}$ on the $A\{\alpha\}$ face are not prescribed, except the requirement that they be compatible with the tangential derivatives on the adjoining $A\{\beta\}$ faces. The complete interior solutions for $\delta \bar{g}_{ab}$ that are compatible with these boundary conditions can be determined in a variety of ways. For example the three-dimensional Laplace equation could be solved for each component of $\delta \bar{g}_{ab}$ with the Dirichlet boundary conditions $\delta \bar{g}_{ab}^{(\alpha)}$ prescribed by the solutions to Eq. (59).

This study has adopted the computationally more efficient approach described in Sec. 3.1. This approach extrapolates the values of $\delta \bar{g}_{ab}^{(\alpha)}$ from the $A\{\alpha\}$ face into the interior using expressions of the form $\delta \bar{g}_{ab} = h(s_A^\alpha) \delta \bar{g}_{ab}^{(\alpha)}$, where the smooth function $h(s)$ is defined in Eq. (5), and s_A^α is defined in Eq. (22). The values of each component of $\delta \bar{g}_{ab}^{(\alpha)}$ vanish on each edge of \mathcal{B}_A because of the boundary conditions, Eq. (55), imposed on the solutions to Eq. (59). It follows that the extrapolations $\delta \bar{g}_{ab} = h(s_A^\alpha) \delta \bar{g}_{ab}^{(\alpha)}$ from the $A\{\alpha\}$ face will vanish on all the other faces of the multicube structure. These face extrapolations can therefore be combined to give a complete interior solution for $\delta \bar{g}_{ab}$ in region \mathcal{B}_A ,

$$\delta \bar{g}_{ab} = \sum_{\alpha} h(s_A^\alpha) \delta \bar{g}_{ab}^{(\alpha)}, \quad (60)$$

that automatically satisfies all the required Dirichlet boundary conditions. Adding the resulting metric perturbation to \bar{g}_{ab} results in a new metric $\bar{\bar{g}}_{ab}$:

$$\bar{\bar{g}}_{ab} = \bar{g}_{ab} + \delta \bar{g}_{ab}. \quad (61)$$

The boundary conditions imposed on $\delta \bar{g}_{ab}$ in this construction ensure that $\bar{\bar{g}}_{ab}$ satisfies the two important properties outlined at the beginning of this subsection. In particular, the intrinsic components of $\bar{\bar{g}}_{ab}$ are identical to those of \bar{g}_{ab} on each cube face, and the boundary conditions imposed on $\delta \bar{g}_{ab}$ ensure that the extrinsic curvatures, $\bar{\bar{K}}_{ab}^{(\alpha)}$, vanish identically along each edge of each cube.

3.3. Step 3: convert $\bar{\bar{g}}_{ab}$ into \tilde{g}_{ab}

Let $\bar{\bar{g}}_{ab}$ denote the global C^0 metric constructed in Sec. 3.2. The goal of this third step is to convert $\bar{\bar{g}}_{ab}$ into a metric \tilde{g}_{ab} having two important properties: first, the extrinsic curvatures $\tilde{K}_{ab}^{(\alpha)}$ associated with \tilde{g}_{ab} must vanish identically on each face of each cubic region; and second, the metric \tilde{g}_{ab} must be identical to $\bar{\bar{g}}_{ab}$ on each face of each cubic region. We note that while $\bar{\bar{g}}_{ab}$ was constructed to have intrinsic parts that are only C^0 across the interface boundaries, within each region $\bar{\bar{g}}_{ab}$ is actually smooth.

We define the unit normal vectors $\tilde{n}_a^{(\alpha)}$, the projection tensors $\tilde{P}_a^{(\alpha)b}$, and the extrinsic curvatures $\tilde{K}_{ab}^{(\alpha)}$ associated with the metric \tilde{g}_{ab} using expressions analogous to those given in Eqs. (24)–(27). Similarly, we define the differences between the \tilde{g}_{ab} and $\bar{\bar{g}}_{ab}$ metrics, $\delta\bar{\bar{g}}_{ab}$, and the associated differences between extrinsic curvatures, $\delta\bar{\bar{K}}_{ab}^{(\alpha)}$:

$$\delta\bar{\bar{g}}_{ab} = \tilde{g}_{ab} - \bar{\bar{g}}_{ab}, \quad (62)$$

$$\delta\bar{\bar{K}}_{ab}^{(\alpha)} = \tilde{K}_{ab}^{(\alpha)} - \bar{\bar{K}}_{ab}^{(\alpha)}. \quad (63)$$

We note that these differences are not assumed to be small. To ensure that \tilde{g}_{ab} is identical to $\bar{\bar{g}}_{ab}$ on the cube faces, we choose $\delta\bar{\bar{g}}_{ab}$ to be a smooth tensor in the interior of each cubic region that satisfies

$$\delta\bar{\bar{g}}_{ab} = 0 \quad (64)$$

on each cube face $A\{\alpha\}$. The condition that the extrinsic curvature $\tilde{K}_{ab}^{(\alpha)}$ vanishes on the $A\{\alpha\}$ face is equivalent to the following condition on $\delta\bar{\bar{K}}_{ab}^{(\alpha)}$,

$$\delta\bar{\bar{K}}_{ab}^{(\alpha)} = -\bar{\bar{K}}_{ab}^{(\alpha)}. \quad (65)$$

In analogy with Eq. (27), an exact expression for $\tilde{K}_{ab}^{(\alpha)}$ is given by

$$\tilde{K}_{ab}^{(\alpha)} = \frac{1}{2} \tilde{P}_a^{(\alpha)c} \tilde{P}_b^{(\alpha)d} \tilde{n}^{(\alpha)e} (\partial_e \tilde{g}_{cd} - \partial_c \tilde{g}_{ed} - \partial_d \tilde{g}_{ec}) \quad (66)$$

$$\begin{aligned} &= \frac{1}{2} \tilde{P}_a^{(\alpha)c} \tilde{P}_b^{(\alpha)d} \tilde{n}^{(\alpha)e} (\partial_e \bar{\bar{g}}_{cd} - \partial_c \bar{\bar{g}}_{ed} - \partial_d \bar{\bar{g}}_{ec}) \\ &\quad + \frac{1}{2} \tilde{P}_a^{(\alpha)c} \tilde{P}_b^{(\alpha)d} \tilde{n}^{(\alpha)e} (\partial_e \delta\bar{\bar{g}}_{cd} - \partial_c \delta\bar{\bar{g}}_{ed} - \partial_d \delta\bar{\bar{g}}_{ec}). \end{aligned} \quad (67)$$

The metric perturbation $\delta\bar{\bar{g}}_{ab}$ vanishes on each cube face, Eq. (64), therefore $\tilde{n}^{(\alpha)a} = \bar{\bar{n}}^{(\alpha)a}$ and $\tilde{P}_a^{(\alpha)b} = \bar{\bar{P}}_a^{(\alpha)b}$ on those faces as well. Consequently, Eq. (67) can be re-written as an exact expression for $\delta\bar{\bar{K}}_{ab}^{(\alpha)}$ on those faces:

$$\delta\bar{\bar{K}}_{ab}^{(\alpha)} = \frac{1}{2} \bar{\bar{P}}_a^{(\alpha)c} \bar{\bar{P}}_b^{(\alpha)d} \bar{\bar{n}}^{(\alpha)e} (\partial_e \delta\bar{\bar{g}}_{cd} - \partial_c \delta\bar{\bar{g}}_{ed} - \partial_d \delta\bar{\bar{g}}_{ec}) \quad (68)$$

$$= \frac{1}{2} (\bar{\bar{N}}^{(\alpha)})^{-1} \bar{\bar{P}}_a^{(\alpha)c} \bar{\bar{P}}_b^{(\alpha)d} \partial_\alpha \delta\bar{\bar{g}}_{cd}. \quad (69)$$

The second equality, Eq. (69), follows from the fact that $\delta\bar{\bar{g}}_{ab}$ vanishes on the $A\{\alpha\}$ face. This implies that $\partial_\beta \delta\bar{\bar{g}}_{ab} = \partial_\gamma \delta\bar{\bar{g}}_{ab} = 0$, $\bar{\bar{P}}_a^{(\alpha)b} \bar{\bar{n}}_b^{(\alpha)} = 0$ so $\bar{\bar{P}}_a^{(\alpha)\alpha} = 0$, and $\bar{\bar{n}}^{(\alpha)\alpha} = (\bar{\bar{N}}^{(\alpha)})^{-1}$.

Let $\mathcal{N}_{ab}^{(\alpha)}$ denote the boundary conditions on $\partial_\alpha \delta\bar{\bar{g}}_{ab}^{(\alpha)}$ on the $A\{\alpha\}$ face. Only the intrinsic components of $\delta\bar{\bar{g}}_{ab}$ contribute to the right side of Eq. (69). Therefore Eqs. (65) and (69) provide the needed boundary conditions for the intrinsic metric components:

$$\partial_\alpha \delta\bar{\bar{g}}_{\beta\beta}^{(\alpha)} = \mathcal{N}_{\beta\beta}^{(\alpha)} = -2\bar{\bar{N}}^{(\alpha)} \bar{\bar{K}}_{\beta\beta}^{(\alpha)}, \quad (70)$$

$$\partial_\alpha \delta\bar{\bar{g}}_{\beta\gamma}^{(\alpha)} = \mathcal{N}_{\beta\gamma}^{(\alpha)} = -2\bar{\bar{N}}^{(\alpha)} \bar{\bar{K}}_{\beta\gamma}^{(\alpha)}, \quad (71)$$

$$\partial_\alpha \delta\bar{\bar{g}}_{\gamma\gamma}^{(\alpha)} = \mathcal{N}_{\gamma\gamma}^{(\alpha)} = -2\bar{\bar{N}}^{(\alpha)} \bar{\bar{K}}_{\gamma\gamma}^{(\alpha)}. \quad (72)$$

The normal derivatives specified in Eqs. (70)–(72) vanish along the edges of the $A\{\alpha\}$ face, because $\bar{\bar{K}}_{ab}^{(\alpha)}$ was constructed to vanish along those edges. These edge conditions are needed to ensure that the normal derivatives $\partial_\alpha \delta\bar{\bar{g}}_{ab}^{(\alpha)}$ are consistent along the $A\{\alpha\beta\}$ edge with the tangential derivatives $\partial_\alpha \delta\bar{\bar{g}}_{ab}^{(\beta)}$ from the adjoining $A\{\beta\}$ face.

The normal derivative boundary conditions on the intrinsic components of $\delta\bar{\bar{g}}_{ab}^{(\alpha)}$ in Eqs. (70)–(72) are sufficient to guarantee that the entire extrinsic curvature vanishes, $\tilde{K}_{ab} = 0$, on the $A\{\alpha\}$ face. The boundary conditions on the gauge components are not fixed in this way, however. These gauge boundary conditions can be chosen arbitrarily so long as they vanish along each cube edge. One choice is simply to set $0 = \mathcal{N}_{\alpha\alpha}^{(\alpha)} = \mathcal{N}_{\alpha\beta}^{(\alpha)} = \mathcal{N}_{\alpha\gamma}^{(\alpha)}$ everywhere on the $A\{\alpha\}$ face. Somewhat

better numerical convergence can be achieved, however, by choosing $\mathcal{N}_{ab}^{(\alpha)}$ to make the second derivatives $\partial_\alpha \partial_\beta \delta \bar{g}_{ab}^{(\alpha)}$ consistent along the $\{\alpha\beta\}$ edge with their values on the adjacent $A\{\beta\}$ face. These conditions on $\mathcal{N}_{ab}^{(\alpha)}$ along the $\{\alpha\beta\}$ edge require

$$\partial_\beta \mathcal{N}_{\alpha\alpha}^{(\alpha)} = \partial_\alpha \mathcal{N}_{\alpha\alpha}^{(\beta)} = -2\partial_\alpha \left(\bar{N}^{(\beta)} \bar{K}_{\alpha\alpha}^{(\beta)} \right), \quad (73)$$

$$\partial_\beta \mathcal{N}_{\alpha\beta}^{(\alpha)} = 0, \quad (74)$$

$$\partial_\beta \mathcal{N}_{\alpha\gamma}^{(\alpha)} = \partial_\alpha \mathcal{N}_{\alpha\gamma}^{(\beta)} = -2\partial_\alpha \left(\bar{N}^{(\beta)} \bar{K}_{\alpha\gamma}^{(\beta)} \right). \quad (75)$$

Analogous conditions on each edge of the $A\{\alpha\}$ face provide Neumann boundary conditions for the gauge components of $\mathcal{N}_{ab}^{(\alpha)}$ along the edges of this face. Together with the Dirichlet conditions $\mathcal{N}_{ab}^{(\alpha)} = 0$ along these edges, they provide the boundary conditions needed to determine $\mathcal{N}_{\alpha\alpha}^{(\alpha)}$, $\mathcal{N}_{\alpha\beta}^{(\alpha)}$, and $\mathcal{N}_{\alpha\gamma}^{(\alpha)}$ everywhere on this face by solving the two-dimensional bi-harmonic equations

$$\left(\partial_\beta^4 + 2\partial_\beta^2 \partial_\gamma^2 + \partial_\gamma^4 \right) \mathcal{N}_{\alpha\alpha}^{(\alpha)} = 0, \quad (76)$$

$$\left(\partial_\beta^4 + 2\partial_\beta^2 \partial_\gamma^2 + \partial_\gamma^4 \right) \mathcal{N}_{\alpha\beta}^{(\alpha)} = 0, \quad (77)$$

$$\left(\partial_\beta^4 + 2\partial_\beta^2 \partial_\gamma^2 + \partial_\gamma^4 \right) \mathcal{N}_{\alpha\gamma}^{(\alpha)} = 0. \quad (78)$$

The pseudo-spectral numerical methods used in this study to solve this equation are described in Appendix B.

Equation (64) provides Dirichlet boundary conditions for $\delta \bar{g}_{ab}$, and the $\mathcal{N}_{ab}^{(\alpha)}$ from Eq. (70)–(72) together with the solutions to Eqs. (76)–(78) provide Neumann boundary conditions on each face of each cubic region. The perturbations $\delta \bar{g}_{ab}$ can therefore be determined throughout the region by solving the three-dimensional biharmonic equation,

$$\left(\partial_x^4 + \partial_y^4 + \partial_z^4 + 2\partial_x^2 \partial_y^2 + 2\partial_x^2 \partial_z^2 + 2\partial_y^2 \partial_z^2 \right) \delta \bar{g}_{ab} = 0, \quad (79)$$

with these boundary conditions. The pseudo-spectral numerical methods used here to solve Eq. (79) for $\delta \bar{g}_{ab}$ are discussed in Appendix B. Adding the resulting $\delta \bar{g}_{ab}$ to \bar{g}_{ab} results in the new metric \tilde{g}_{ab} :

$$\tilde{g}_{ab} = \bar{g}_{ab} + \delta \bar{g}_{ab}. \quad (80)$$

The boundary conditions imposed on $\delta \bar{g}_{ab}$ ensure that \tilde{g}_{ab} satisfies the two important properties outlined at the beginning of this subsection; namely, the components of \tilde{g}_{ab} are identical to those of \bar{g}_{ab} on each cube face, and the extrinsic curvatures, $\tilde{K}_{ab}^{(\alpha)}$, vanish identically on each cube face. It follows that the intrinsic components of \tilde{g}_{ab} and the extrinsic curvatures $\tilde{K}_{ab}^{(\alpha)}$ are continuous across the interface boundaries between all the cubic regions. Therefore \tilde{g}_{ab} satisfies the Israel [8] junction conditions across all the boundaries of the multicube structure, and is therefore C^1 globally.

4. Numerical examples

Multicube structures for a collection of manifolds have been developed here to test the numerical reference metric construction methods described in Secs. 2 and 3. All the multicube structures used in these examples satisfy the local reflection symmetry property described in Sec. 2. This condition is needed to permit the construction of flat metrics in the neighborhood of each vertex having uniform dihedral angles around each edge of the cubic regions. These example manifolds are listed in Table 2, including their Thurston geometrization classes (see Ref. [17]). They include representatives from five of the eight Thurston geometrization classes, missing only the SL_2 , Nil , and Sol classes.

Some of the multicube structures used in these examples were constructed by hand, while most were constructed from triangulations obtained from Ref. [6] using the method developed in Ref. [1]. The multicube structures constructed from triangulations were done automatically by the code described in Appendix A. Those constructed by hand include the Three-Torus (E1), S3 and $S \times S1$, as described in Ref. [1]. Manifolds of the form $G_n \times S^1$, where G_n is the compact orientable two-manifold with genus number n , can be constructed easily by hand from the two-dimensional multicube structures developed for arbitrary G_n in Ref. [7]. This study includes $G_2 \times S1$ as an example. Multicube structures have also been constructed by hand for several manifolds that can be defined by identifying the faces of three-dimensional polygonal solids. The numerical examples presented here include the Poincaré dodecahedral space [11], Seifert-Weber space [12], and all six compact orientable three-manifolds that admit flat metrics (sometimes called E1-E6) [13,14], and the Hantzsche-Wendt space [15] (also called E6). Appendix D gives the complete descriptions of the previously unpublished multicube structures constructed by hand for this study, along with a representative selection of those constructed automatically from triangulations by the code described in Appendix A.

Reference metrics \tilde{g}_{ab} have been constructed numerically for each of the manifolds listed in Table 2. The methods developed in Secs. 2 and 3 are designed to make the intrinsic parts of \tilde{g}_{ab} continuous across the interface boundaries

Table 2

Manifolds used in numerical tests of the C^1 metric construction methods developed in Secs. 2 and 3. First part of the table lists this multicube structures constructed by hand, while the second part lists those constructed from triangulations by the code described in Appendix A. Names used for the manifolds constructed from triangulations are those used in Ref. [6]. The $L(p,q)$ manifolds are lens spaces, i.e., quotients of the three-sphere S^3 with a discrete group characterized by parameters (p,q) . The manifolds $S^2 \times S^1$, $T \times S^1$, $KB/n2 \times \sim S^1$, and $SFS[B : (p_1, q_1)(p_2, q_2)(p_3, q_3)]$, are Seifert fibered spaces. S^1 represents a circle. The \times operator is the Cartesian product, e.g. $S^2 \times S^1$, while $\times \sim$ is the twisted product used to undo the non-orientability of the base manifold, e.g. in $KB/n2 \times \sim S^1$. The base spaces B include the two-sphere S^2 , the real projective plane $RP^2/n2$, the Klein bottle $KB/n2$, and the two-torus T . The parameters, e.g. (p_1, q_1) , describe “singular” fibers whose neighborhoods have been replaced by fibers twisted by an amount determined by (p_1, q_1) .

Three-dimensional multicube structures constructed by hand					
Manifold		Geometry class	Manifold		Geometry class
Three-Torus (E1)		E^3	Half-Turn Space (E2)		E^3
Quarter-Turn Space (E3)		E^3	Third-Turn Space (E4)		E^3
Sixth-Turn Space (E5)		E^3	Hantzsche-Wendt Space (E6)		E^3
Three-Sphere (S3)		S^3	$S^2 \times S^1$		$S^2 \times S^1$
$G2 \times S^1$		$H^2 \times S^1$	Seifert-Weber Space		H^3
Poincaré Dodecahedral Space		S^3			

Three-dimensional multicube structures constructed from triangulations					
Manifold	Geometry class	Manifold	Geometry class	Manifold	Geometry class
$L(5, 2)$	S^3	$L(40, 19)$	S^3	$SFS[S2 : (2, 1)(2, 1)(7, -6)]$	S^3
$L(8, 3)$	S^3	$L(44, 21)$	S^3	$SFS[S2 : (2, 1)(2, 1)(8, -7)]$	S^3
$L(10, 3)$	S^3	$T \times S^1$	E^3	$SFS[S2 : (2, 1)(2, 1)(9, -8)]$	S^3
$L(12, 5)$	S^3	$KB/n2 \times \sim S^1$	E^3	$SFS[S2 : (2, 1)(2, 1)(10, -9)]$	S^3
$L(16, 7)$	S^3	$SFS[RP^2/n2 : (2, 1)(2, -1)]$	E^3	$SFS[S2 : (2, 1)(2, 1)(11, -10)]$	S^3
$L(20, 9)$	S^3	$SFS[S2 : (2, 1)(2, 1)(2, -1)]$	S^3	$SFS[S2 : (2, 1)(3, 1)(5, -4)]$	S^3
$L(24, 11)$	S^3	$SFS[S2 : (2, 1)(2, 1)(3, -2)]$	S^3	$SFS[S2 : (2, 1)(3, 2)(3, -1)]$	S^3
$L(28, 13)$	S^3	$SFS[S2 : (2, 1)(2, 1)(4, -3)]$	S^3	$SFS[S2 : (2, 1)(4, 1)(4, -3)]$	S^3
$L(32, 15)$	S^3	$SFS[S2 : (2, 1)(2, 1)(5, -4)]$	S^3	$SFS[S2 : (3, 1)(3, 1)(3, -2)]$	S^3
$L(36, 17)$	S^3	$SFS[S2 : (2, 1)(2, 1)(6, -5)]$	S^3		

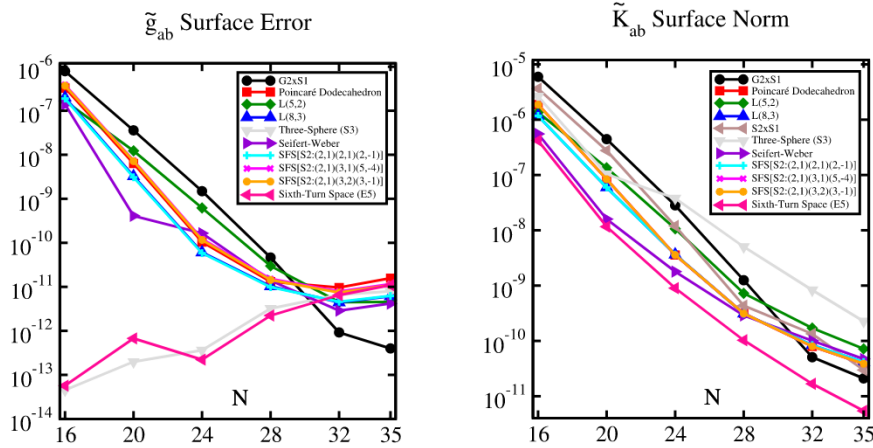


Fig. 5. Graphs representing L_2 norms, for different values of the spatial resolution N , of the intrinsic metric discontinuities of \tilde{g}_{ab} across the multicube interface boundaries in the left Fig. 5(a), and L_2 norms of the associated extrinsic curvatures $\tilde{K}_{ab}^{(\alpha)}$ of those boundaries in the right Fig. 5(b). In Fig. 5(a) the graph for $S^2 \times S^1$ is not shown because the errors are at the 10^{-15} level.

between the cubic regions, and also to make the associated extrinsic curvatures, $\tilde{K}_{ab}^{(\alpha)}$, vanish on each interface boundary. These conditions satisfy the Israel junction conditions [8] that ensure \tilde{g}_{ab} is C^1 across those interfaces.

The methods introduced in Secs. 2 and 3 have been implemented numerically for this study in the SpEC pseudo-spectral code (developed originally by the Caltech/Cornell numerical relativity collaboration [18–20]). Figs. 5 and 6 show L_2 norms of the surface discontinuities of the intrinsic parts of \tilde{g}_{ab} and the extrinsic curvatures $\tilde{K}_{ab}^{(\alpha)}$ as functions of the spatial resolution parameter N (the number of spectral collocation points used in each dimension) for most of the manifolds listed in Table 2. These L_2 norms were computed by averaging the squares of all the intrinsic components of each tensor over all the grid points on all interface surfaces, and finally taking the square root of this average. These results show that the numerical methods developed and implemented here produce C^1 reference metrics having small errors that converge toward satisfying the Israel junction conditions as the spatial resolution is increased. The results for the manifolds not included in these graphs are similar to those shown in Fig. 6 (except for the flat manifolds E1-E4 and E6 whose \tilde{K}_{ab} errors are at or below the 10^{-12} level for all N).

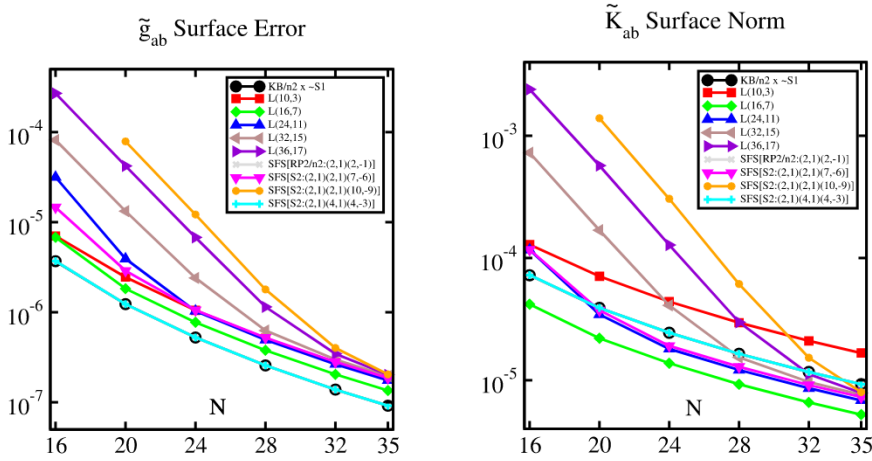


Fig. 6. Graphs representing L_2 norms, for different values of the spatial resolution N , of the intrinsic metric discontinuities of \tilde{g}_{ab} across the multicube interface boundaries in the left Fig. 6(a), and L_2 norms of the associated extrinsic curvatures $\tilde{K}_{ab}^{(\alpha)}$ of those boundaries in the right Fig. 6(b).

The results of these numerical tests have been divided into two groups. Those represented in Fig. 5 have significantly smaller errors than those shown in Fig. 6. The reason for these differences appears to be the amount of distortion caused by the dihedral angles needed to allow the cubic regions to fit together without introducing conical edge singularities. Higher resolutions are needed to represent models having larger distortions at a particular accuracy level. All the manifolds in the larger error group, Fig. 6, have some edges with small dihedral angles, $\min(\psi) \leq 2\pi/6$, while those in the smaller error group, Fig. 5, have larger minimum dihedral angles $\min(\psi) \geq 2\pi/5$ (except for $G_2 \times S^1$ and Sixth-Turn Space, E5, which have $\min(\psi) = 2\pi/6$).

The surface errors in \tilde{g}_{ab} and \tilde{K}_{ab} for the examples shown in Fig. 5 decrease (approximately) exponentially with increasing N for $N \leq 28$. Double precision roundoff error is probably limiting convergence in these cases for $N > 28$. Some of the examples in Fig. 6 also show exponential convergence for $N \leq 28$. However most of the examples in Fig. 6 show slower power law convergence in N . For example the errors in one of the slowest converging cases, $KB/n2 \times S^1$, are well fit by the power laws $N^{-14/3}$ for \tilde{g}_{ab} and $N^{-8/3}$ for $\tilde{K}_{ab}^{(\alpha)}$. There is some indication that the examples in Fig. 6 with exponential convergence transition to power law convergence for larger values of N . This transition is probably caused by errors due to discontinuities in the mixed partial derivatives of $\delta\tilde{g}_{ab}$ at some of the edges. These discontinuities are caused by disagreements between the tangential derivatives of the Neumann boundary data on the faces that intersect along those edges. At some resolution these higher-order discontinuity errors become dominant and power law convergence takes over. The examples in Fig. 6 with the largest errors are also those with the most distorted multicube structures, some with dihedral angles as small as $\min(\psi) = 2\pi/8$. This supports the idea that the larger distortions cause the larger errors at a given resolution N .

5. Discussion

New methods have been presented in Secs. 2 and 3 for building three-dimensional differentiable manifolds numerically. These methods involve the construction of C^1 reference metrics that are used to construct special Jacobians to define the continuity of tensors, and a covariant derivative to define the differentiability of those tensors, across the interface boundaries between coordinate charts. These methods have been applied in Sec. 4 to a selection of forty three-dimensional manifolds, including examples from five of the eight Thurston geometrization classes. Test results on these examples show that the methods developed in Secs. 2 and 3, and our implementation of those methods in the SpEC pseudo-spectral code, are numerically convergent.

The methods developed here are general enough to be applied to a larger variety of differentiable three-manifolds than has been studied previously using existing numerical methods. However, the methods presented here make very restrictive assumptions about the multicube structures to which they can be applied. Perhaps the most obvious limitation is the assumption in Sec. 2 that the multicube structure exhibits a particular local reflection symmetry. A diverse collection of manifolds that satisfy this restriction has been constructed, however, this assumption is not satisfied by most multicube structures. We do not think that this assumption is essential. It was made here because it was easy to implement numerically in our code. We think it will be possible to relax this assumption. We plan to investigate ways to do that in a future study.

Another obvious limitation of the results presented in Sec. 4 is the relatively slow numerical convergence of the reference metrics constructed on manifolds having highly distorted multicube structures. One significant part of this problem is probably caused by the discontinuities in the derivatives of the Neumann boundary data used to determine the C^1 reference metrics in Sec. 3.3 (at cube edges where some intrinsic metric component is present on both faces, e.g. the $\tilde{g}_{\gamma\gamma}$ component along the $A\{\alpha\beta\}$ edge). We think this particular problem can be ameliorated by enforcing somewhat different

boundary conditions on the gauge components of the metric in Sec. 3.2. We plan to investigate this and other approaches to improving the numerical convergence of these methods in a future study.

Most of the differential equations used in the physical sciences, e.g. systems of symmetric hyperbolic evolution equations, or systems of second-order elliptic equations, require specifying some combination of the values of fields and their derivatives at the boundaries of computational domains. The C^1 reference metrics developed in this paper are sufficient to provide the needed transformations of these data at the interface boundaries between coordinate patches. We showed in Ref. [7] that the differentiable structures produced by different C^1 reference metrics are equivalent. The needed continuity of the boundary data at the interfaces between computational domains can therefore be done correctly and exactly using the C^1 reference metrics constructed here. There is no fundamental need to refine these reference metrics by increasing their global differentiability.

For various reasons it may be desirable, however, to transform these metrics further to produce metrics that are smoother at the interface boundaries, or perhaps that have more uniform spatial structures which can be resolved numerically at lower resolutions. In Ref. [7] we used numerical Ricci flow to evolve the C^1 reference metrics developed there for two-dimensional manifolds. Ricci flow is a system of parabolic evolution equations that transform C^1 initial data into C^∞ solutions at later times [21–25]. The initial metrics for Ricci flow are required to have bounded curvatures [26,27] to ensure that even very short evolutions become real analytic. The Israel junction conditions [8] guarantee that while our C^1 reference metrics may have curvature discontinuities across the interfaces, they will not be unbounded there. Ricci flow in two dimensions also evolves all initial data into constant curvature geometries. We plan to use numerical Ricci flow to evolve the three-dimensional C^1 reference metrics produced here in a future study. In three dimensions, Ricci flow may form singularities before the manifold attains constant curvature, even for manifolds like the Three-Sphere (S^3) having very simple topologies [28]. While there is no guarantee that the Ricci flow of our C^1 metrics will necessarily produce more uniform geometries, it will be interesting to see what happens. If singularities occur then it will be interesting to explore the nature of those singularities. If these evolutions proceed to uniform curvature solutions, then it will be interesting to determine and to verify that the resulting geometries satisfy the appropriate properties associated with their Thurston geometrization classes.

Finally, we plan to use the reference metrics developed here in a future study to solve Einstein's equations numerically on a diverse collection of manifolds. Solving Einstein's equations involves finding solutions to an elliptic system to obtain acceptable initial data, and then to evolve those data using a system of hyperbolic equations that determine the structure of the resulting spacetime. The appropriate representation of Einstein's equations to use in spacetimes with non-trivial topologies was developed in Ref. [29]. We plan to use those methods to explore solutions representing cosmological models evolved from initial data on a diverse collection of compact three-manifolds. It might also be interesting to explore solutions to Einstein's equations on manifolds with non-trivial topologies and asymptotically flat initial data. These geometries are expected to evolve into black-hole spacetimes [30–32], with any non-trivial topological structures hidden behind event horizons. By studying these evolutions, it will be interesting to explore whether observers outside the black holes could identify the presence of these topological structures in some indirect way.

CRedit authorship contribution statement

Lindblom played the major role in all aspects of this project from the conceptualization and methodology development, formal analysis, software development and implementation, and the manuscript writing and editing.

Rinne played a major role in the ideas and development of the Python code used to transform triangulations into multicube structures. He also played an important role in checking and editing the formal analysis, and in the final editing of the manuscript and in preparing the responses to the referees.

Taylor played an important role in helping in the implementation of these ideas into the SpEC code, and in debugging various problems that arose during that implementation. He also played a role in editing the original version of the manuscript for submission.

Declaration of competing interest

The authors declare that they have no known competing financial interests or personal relationships that could have appeared to influence the work reported in this paper.

Acknowledgements

This research was supported in part by NSF grant 2012857 to the University of California at San Diego.

Appendix A. Converting three-manifold triangulations to multicube structures

This appendix describes the method used by our code to convert a three-dimensional triangulation into a multicube structure. A three-dimensional triangulation consists of a set of tetrahedra and the identification maps that identify each tetrahedron face with the appropriate face of its neighbor. These face identifications are determined by specifying which

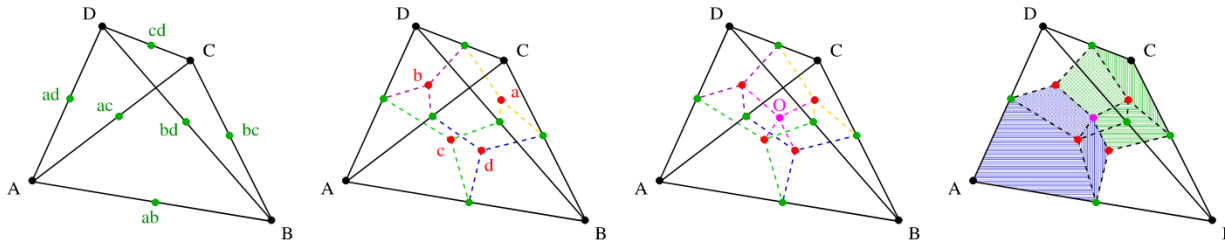


Fig. A.1. In Fig. A.1(a) label the vertices of the tetrahedron “A”, “B”, “C” and “D”, and add vertices at the midpoints of each edge. In Fig. A.1(b) add additional vertices at the centroid of each face of the tetrahedron, labeled “a” for the centroid of face “BCD”, “b” for face “ACD”, etc. Then add additional edges (shown as dashed line segments) connecting each centroid to the midpoint of each adjoining edge. In Fig. A.1(c) add one additional vertex, labeled “O” at the centroid of the tetrahedron. Add additional edges (shown as dash-dot line segments) that connect “O” to the centroids of each face, and add six additional faces that include “O” as a vertex. In Fig. A.1(d) the “distorted” cubes that make up the tetrahedron are illustrated. The two cubes adjacent to vertices “A” and “C” are shown with opaque shaded faces, while the faces of the cubes adjacent to “B” and “D” are transparent.

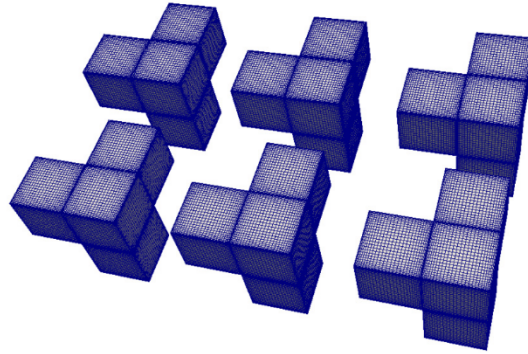


Fig. A.2. Locations of the cubic regions in \mathbb{R}^3 assigned by our code for the manifold SFS[RP2/n2:(2,1)(2,-1)] based on the triangulation given in the Regina [6] catalog. Each tetrahedron is divided into four cubes, which are placed in groups with some of the identified internal faces overlapping.

vertices of one tetrahedron are identified with which vertices of its neighbor. Large numbers of triangulations specified in this way are published in the Regina catalog [6]. Our code is designed to read the triangulation structures exported into files by the Regina software.

Given a three-dimensional triangulation, it is straightforward to convert it to a multicube structure following the method described in Ref. [1]. The idea is to cut each tetrahedron into four cubes by adding vertices and edges as illustrated in Fig. A.1, and described in some detail in the caption. Our code creates a list of cubic regions from the list of tetrahedrons, then it assigns unique locations in \mathbb{R}^3 to each cube. These locations are chosen so the four cubes associated with each tetrahedron are grouped together, and these tetrahedron based groups are arranged in a 2D lattice for convenience of 3D visualization. Fig. A.2 illustrates the locations of the cubes assigned by our code for the multicube structure constructed for the SFS[RP2/n2:(2,1)(2,-1)] manifold from the triangulation given in the Regina catalog.

Finally our code constructs the appropriate maps in \mathbb{R}^3 between cube faces using Eq. (D.1), following the prescription given in Ref. [29]. In addition to the locations of each cube, these maps depend on knowing the appropriate rotation/reflection matrix, $C_{B\beta}^{A\alpha}$, that aligns the faces $A\{\alpha\}$ and $B\{\beta\}$ in the appropriate way. Each cube has six faces, three of which correspond to internal connections between the four cubes that make up a tetrahedron. The rotation/reflection matrices needed for these internal face transformations are the same for every tetrahedron group of cubes. So they are easily included in the code. The three additional faces of each cube are parts of the faces of the tetrahedra. The appropriate rotation/reflection matrices for those faces depend on the face mappings of the triangulations. There are, however, a reasonably small number of ways the faces of any two tetrahedra can be identified. Our code includes the appropriate matrices for all the possible cube face matchings (which we determined by systematically reproducing each possibility with a collection of paper models). Once a triangulation with its face mappings is read into our code, it automatically determines the appropriate cube mappings from its table of all possibilities. Our code can then output the complete multicube structure in any desired format. For example Tables D.6, D.8, D.9 and D.10 in Appendix D are output from our code in \LaTeX format. Our code also generates the appropriately formatted input files used by the SpEC code to compute the reference metrics \tilde{g}_{ab} described in Sec. 4.

Our code can be used to construct a multicube structure from any three-dimensional triangulation. However, the methods for constructing reference metrics presented in Sec. 2 only work for special multicube structures that allow uniform dihedral angles around each edge. The code therefore tests several identities to determine when this is possible.

Once the multicube structure has been constructed by the code, it determines the dihedral angles $\psi_{A\{\alpha\beta\}}$ around each edge using the uniform dihedral angle assumption given in Eq. (1) of Sec. 2.2. The most important identity that must be

satisfied by these $\psi_{A\{\alpha\beta\}}$ involves the associated angles $\theta_{A\{\alpha\}}$ between the axes that define the edges of the $A\{\alpha\}$ face. These angles must agree with the angles $\theta_{B\{\alpha\}}$ between the axes of the $B\{\alpha\}$ face identified with it in the multicube structure. Without this condition the intrinsic metric of region \mathcal{B}_A would not be continuous across that face with the intrinsic metric of region \mathcal{B}_B . The edge angle $\theta_{A\{\alpha\}}$ is related to the dihedral angles $\psi_{A\{\alpha\beta\}}$ using the spherical law of cosines,

$$\cos \theta_{A\{\alpha\}} = \frac{\cos \psi_{A\{\beta\gamma\}} + \cos \psi_{A\{\alpha\beta\}} \cos \psi_{A\{\alpha\gamma\}}}{\sin \psi_{A\{\alpha\beta\}} \sin \psi_{A\{\alpha\gamma\}}}. \quad (\text{A.1})$$

Our code evaluates the $\theta_{A\{\alpha\}}$ for each vertex of each cube face and determines whether it agrees with the corresponding angles $\theta_{B\{\alpha\}}$ at those vertices. Multicube structures that do not satisfy this condition could not be used in the present study.

Our code also checks two other less restrictive identities. One ensures that the determinant of the flat inverse metric $e_{A\{\alpha\beta\gamma\}}^{ab}$ defined in Eq. (2) is positive in each cubic region:

$$\det e_{A\{\alpha\beta\gamma\}}^{ab} = 1 + 2 \cos \psi_{A\{\alpha\beta\}} \cos \psi_{A\{\alpha\gamma\}} \cos \psi_{A\{\beta\gamma\}} - \cos^2 \psi_{A\{\alpha\beta\}} - \cos^2 \psi_{A\{\alpha\gamma\}} - \cos^2 \psi_{A\{\beta\gamma\}} > 0. \quad (\text{A.2})$$

A second identity ensures that the areas of the spherical triangles created by the intersection of each cubic region with small spheres located at their vertices (see Fig. 2(b)) are positive. This requires

$$\psi_{A\{\alpha\beta\}} + \psi_{A\{\alpha\gamma\}} + \psi_{A\{\beta\gamma\}} > \pi. \quad (\text{A.3})$$

We have run this code on all the triangulations consisting of up to eleven tetrahedra listed in the catalogs of all closed prime orientable three-manifolds in Refs. [2–6]. We find that of these only the 29 manifolds listed in Table 2 satisfy all these constraints.

Appendix B. Solving the biharmonic equation using pseudo-spectral methods

The biharmonic equations in two and three dimensions are given by

$$0 = \left(\partial_x^4 + 2 \partial_x^2 \partial_y^2 + \partial_y^4 \right) U, \quad (\text{B.1})$$

$$0 = \left(\partial_x^4 + \partial_y^4 + \partial_z^4 + 2 \partial_x^2 \partial_y^2 + 2 \partial_x^2 \partial_z^2 + 2 \partial_y^2 \partial_z^2 \right) U. \quad (\text{B.2})$$

The solutions to these equations on compact domains are determined uniquely by the values of U and its normal derivative dU/dn (the Dirichlet and Neumann conditions respectively) on the boundaries of the domain [16].

In this study these equations are solved using pseudo-spectral numerical methods. A function U is specified in this approach by its values on a special mesh. The mesh points used here are located at the Gauss-Lobatto collocation points [33]. This choice makes it possible to transform easily and exactly back and forth between the mesh representation and a Chebyshev polynomial based spectral representation of U . The value of U at a particular mesh point is written here as $U_{\{ij\}}$ in two dimensions or $U_{\{ijk\}}$ in three. Partial derivatives of a function, which are exact for this spectral representation, can be written as special linear combinations of its values on these mesh points,

$$\partial_x U_{\{ij\}} = \mathcal{D}^{(x)}_i{}^s U_{\{sj\}}, \quad (\text{B.3})$$

$$\partial_y U_{\{ij\}} = \mathcal{D}^{(y)}_j{}^t U_{\{it\}}, \quad (\text{B.4})$$

where the repeated indices s or t are summed over all the mesh points in the particular direction. The discrete pseudo-spectral representation of the two-dimensional biharmonic equation can therefore be written as

$$0 = \mathcal{D}^{(x)}_i{}^s \mathcal{D}^{(x)}_s{}^t \mathcal{D}^{(x)}_t{}^u \mathcal{D}^{(x)}_u{}^v U_{\{vj\}} + 2 \mathcal{D}^{(x)}_i{}^s \mathcal{D}^{(x)}_s{}^t \mathcal{D}^{(y)}_j{}^u \mathcal{D}^{(y)}_u{}^v U_{\{tv\}} + \mathcal{D}^{(y)}_j{}^s \mathcal{D}^{(y)}_s{}^t \mathcal{D}^{(y)}_t{}^u \mathcal{D}^{(y)}_u{}^v U_{\{iv\}}. \quad (\text{B.5})$$

An analogous expression is used for the discrete representation of the biharmonic equation in three dimensions.

Boundary conditions are imposed by replacing the discrete biharmonic equations along the outer layer of mesh points with discrete versions of the Neumann boundary conditions at those points. Dirichlet boundary conditions are also needed along the boundaries, and those are imposed by replacing the discrete biharmonic equation on the mesh points at the next layer of points adjacent to the boundary with the Dirichlet condition evaluated at the nearest boundary points. Fig. B.1(a) illustrates where these boundary conditions are imposed for the case of a two-dimensional mesh. The three-dimensional case is analogous, but more difficult to illustrate in two-dimensional figures.

The functions $U_{\{ij\}}$ in two dimensions (or $U_{\{ijk\}}$ in three) can be thought of as vectors $U_{\mathcal{A}}$ on a space where the super-index \mathcal{A} ranges over all the mesh points, i.e. $\mathcal{A} = \{ij\}$ in two dimensions (or $\mathcal{A} = \{ijk\}$ in three). The discrete biharmonic equation can be thought of as a linear matrix equation on this space:

$$\sum_{\mathcal{B}} \mathcal{O}_{\mathcal{A}}{}^{\mathcal{B}} U_{\mathcal{B}} = h_{\mathcal{A}}, \quad (\text{B.6})$$

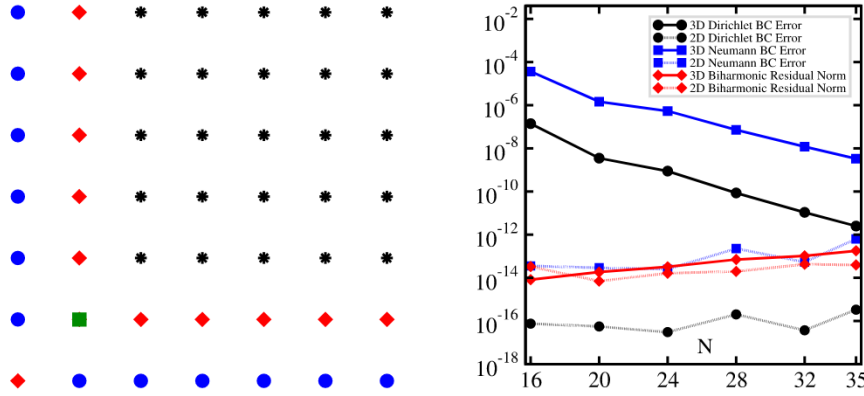


Fig. B.1. Figure on the left represents one corner of a two-dimensional mesh used to solve the biharmonic equation. Discrete representations of the boundary conditions for points along the boundaries replace the biharmonic equation at the points marked with (red) diamonds for Dirichlet and (blue) circles for Neumann conditions, respectively. The average of the Dirichlet conditions from both nearby boundary points is imposed at the point marked with a (green) square. Discrete representations of the biharmonic equation are imposed at the remaining interior mesh points marked with (black) stars. Figure on the right illustrates the average (rms) boundary errors in the Dirichlet and Neumann boundary conditions for examples of the numerical 2D and 3D biharmonic solutions used in this study.

where \mathcal{O}_A^B is defined in two dimensions by the expression in Eq. (B.5) at the interior mesh points. The discrete versions of the Dirichlet and Neumann conditions are imposed on the components of this equation representing the surface layers of the mesh. The vector h_A holds the boundary data for those conditions, in addition (if any) to the inhomogeneous source for the equation at the interior points. The expression used here for \mathcal{O}_A^B in three dimensions is completely analogous.

Our primary interest is finding smooth functions U that satisfy the boundary conditions as accurately as possible. The components of the matrices $\mathcal{D}^{(x)_i^j}$, etc., which provide discrete representations of the derivative operators, have average magnitudes that scale like N , where N is the number of mesh points used in each direction. Therefore the components of the matrix \mathcal{O}_A^B representing the biharmonic operator on interior mesh points will scale like N^4 , and for large N will therefore dominate the boundary condition terms. These interior components have therefore been scaled in this study by N^{-4} to emphasize the relative importance of the boundary conditions. A similar scaling would also be applied to any source terms in h_A , however, no additional scaling is needed for the homogeneous equations considered here.

The linear equations given in Eq. (B.6) can be solved numerically using a variety of iterative techniques, e.g. using solvers such as GMRES [34] or BI-CGSTAB [35]. Numerical experiments using pseudo-spectral methods described above for this problem showed that faster and more accurate results could be obtained using more direct non-iterative methods, because the meshes used here are relatively small (in comparison with those used by standard finite difference or finite element methods). The matrix \mathcal{O}_A^B has size $N^2 \times N^2$ for the two-dimensional problem and $N^3 \times N^3$ for three, where N is the number of mesh points used in each dimension. The largest meshes used in this study have $N = 35$, so the largest matrix has size $1,225 \times 1,225$ for the two-dimensional meshes, and $42,875 \times 42,875$ for three. For matrices of this size, it is possible to construct the LU decomposition of \mathcal{O}_A^B directly using modest computing resources. Very fast direct algorithms then exist for solving such linear systems exactly, see e.g. Ref. [36]. The construction of the LU decomposition requires a lot of memory and computer time. The highest resolution that could be run on the computing facility available to us is $N = 35$ due to memory limitations. Constructing the LU decomposition at this resolution required about 152 hours on a single processor. But once computed for each needed resolution N , these LU decompositions can be stored on disk and quickly read in whenever they are needed. A very accurate solution of the linear equations in LU form can then be obtained very quickly and efficiently. Pre-computing the LU decompositions in this way reduces the $N = 35$ problem of solving one 3D biharmonic equation (plus six 2D biharmonic equations to set the boundary conditions) from about 152 hours to about 75 seconds.

The condition number κ of a matrix operator \mathcal{O}_A^B is a measure of how accurately linear equations like Eq. (B.6) can be solved numerically [37]. Fractional errors in the solutions U_B can be as large as κ multiplied by the fractional errors in the matrix \mathcal{O}_A^B and the source h_A . We have estimated κ for the two and three-dimensional representations of the biharmonic matrices used in our study. These approximations were obtained using the simple approximate expression:

$$\kappa_\infty = \|\mathcal{O}\|_\infty \|\mathcal{O}^{-1}\|_\infty \geq \frac{\max_A \sum_B |\mathcal{O}_A^B|}{\min_A |\mathcal{U}_A^A|}, \quad (\text{B.7})$$

where \mathcal{U}_A^B is the upper diagonal part of the LU decomposition: $\sum_C \mathcal{P}_A^C \mathcal{O}_C^B = \sum_C \mathcal{L}_A^C \mathcal{U}_C^B$, where \mathcal{P}_A^C is a permutation matrix. These estimates of κ_∞ using Eq. (B.7) are illustrated in Fig. B.2. As the figures show, these estimates for the condition number scale with spatial resolution N as a power law: $\sim N^{4.2}$. While condition numbers as large as the 10^5 seen in this figure might seem large, they mean that fractional errors in the matrix \mathcal{O}_A^B and the source h_A at the double precision roundoff level, 10^{-16} , could produce fractional errors only as large as 10^{-11} in the solution U_B . We also note

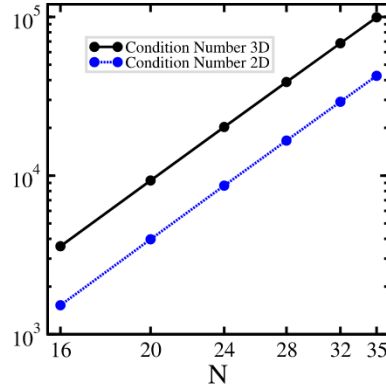


Fig. B.2. Figure illustrates the spatial resolution, N , dependence of the condition number κ_∞ (using the estimate given in Eq. (B.7)) for the pseudo-spectral matrix representations of the two- and three-dimensional biharmonic operators used in this study.

that condition numbers of this size have not significantly influenced the boundary condition errors (our primary interest in these solutions), as illustrated in Figs. B.1(b), 5 and 6.

In addition to being very quick and efficient, the direct LU solver method used here provides solutions having better accuracy for our purposes than those obtained with the iterative solvers that were tested. Solutions to the two- and three-dimensional biharmonic equation are used here at various stages in the construction of a reference metric. The important requirement is the need to have those solutions satisfy the Dirichlet and Neumann boundary conditions as accurately as possible. The interior details are not of primary importance, so long as they are smooth. Fig. B.1(b) illustrates the convergence with resolution N of the errors in the Dirichlet and Neumann boundary conditions satisfied by numerical examples of two- and three-dimensional biharmonic solutions obtained with this direct LU solver method. The two-dimensional results are at the double-precision roundoff levels for all values of N tested, while the three-dimensional results show the exponential convergence that is expected for pseudo-spectral methods. The average interior bulk residual errors are also roughly at double-precision roundoff levels. The boundary condition accuracies achieved using this direct LU solver method were much better than anything obtained with the iterative solvers tested here.

Appendix C. Proof of the identity $\bar{N}^{(\beta)} \bar{K}_{\alpha\gamma}^{(\beta)} = -\bar{N}^{(\alpha)} \bar{K}_{\beta\gamma}^{(\alpha)}$

The following simple argument shows that this condition is satisfied along the $A\{\alpha\beta\}$ edge by the C^0 metric \bar{g}_{ab} constructed in Sec. 3.1. Start with the identity

$$\gamma^a \bar{n}^{(\alpha)b} \bar{K}_{ab}^{(\beta)} = \gamma^a \bar{n}^{(\alpha)b} \bar{\nabla}_a \bar{n}_b^{(\beta)} = \gamma^a \bar{\nabla}_a (\bar{n}^{(\alpha)b} \bar{n}_b^{(\beta)}) - \gamma^a \bar{n}^{(\beta)b} \bar{\nabla}_a \bar{n}_b^{(\alpha)} = -\gamma^a \bar{n}^{(\beta)b} \bar{K}_{ab}^{(\alpha)}, \quad (\text{C.1})$$

where the γ^a are the components of the vector $\partial_\gamma = \gamma^a \partial_a$ that is tangent to both the $A\{\alpha\}$ and $A\{\beta\}$ faces. The last equality follows from the fact that $\partial_\gamma (\bar{n}^{(\alpha)b} \bar{n}_b^{(\beta)}) = 0$ because the dihedral angle is constant along the $A\{\alpha\beta\}$ edge. The additional simple identities $\bar{n}^{(\alpha)a} \gamma^b \bar{K}_{ab}^{(\alpha)} = \bar{n}^{(\beta)a} \gamma^b \bar{K}_{ab}^{(\beta)} = 0$ and $\bar{K}_{\gamma\gamma}^{(\alpha)} = \bar{K}_{\gamma\gamma}^{(\beta)} = 0$ can be used to transform the tensor identity in Eq. (C.1) into the coordinate identity given in Eq. (45). First obtain the coordinate representations of the simple identities:

$$0 = \bar{n}^{(\alpha)a} \gamma^b \bar{K}_{ab}^{(\alpha)} = \bar{N}^{(\alpha)} (\bar{g}^{\alpha\alpha} \bar{K}_{\alpha\gamma}^{(\alpha)} + \bar{g}^{\alpha\beta} \bar{K}_{\beta\gamma}^{(\alpha)}), \quad (\text{C.2})$$

$$0 = \bar{n}^{(\beta)a} \gamma^b \bar{K}_{ab}^{(\beta)} = \bar{N}^{(\beta)} (\bar{g}^{\beta\alpha} \bar{K}_{\alpha\gamma}^{(\beta)} + \bar{g}^{\beta\beta} \bar{K}_{\beta\gamma}^{(\beta)}). \quad (\text{C.3})$$

Coordinate representations of $\bar{n}^{(\beta)a} \gamma^b \bar{K}_{ab}^{(\alpha)}$ and $\bar{n}^{(\alpha)a} \gamma^b \bar{K}_{ab}^{(\beta)}$ can be written as

$$\bar{n}^{(\beta)a} \gamma^b \bar{K}_{ab}^{(\alpha)} = \bar{N}^{(\beta)} (\bar{g}^{\beta\alpha} \bar{K}_{\alpha\gamma}^{(\alpha)} + \bar{g}^{\beta\beta} \bar{K}_{\beta\gamma}^{(\alpha)}), \quad (\text{C.4})$$

$$\bar{n}^{(\alpha)a} \gamma^b \bar{K}_{ab}^{(\beta)} = \bar{N}^{(\alpha)} (\bar{g}^{\alpha\alpha} \bar{K}_{\alpha\gamma}^{(\beta)} + \bar{g}^{\alpha\beta} \bar{K}_{\beta\gamma}^{(\beta)}). \quad (\text{C.5})$$

These expressions can be simplified by using Eq. (C.2) to express $\bar{K}_{\alpha\gamma}^{(\alpha)}$ in terms of $\bar{K}_{\beta\gamma}^{(\alpha)}$, and similarly Eq. (C.3) to express $\bar{K}_{\beta\gamma}^{(\beta)}$ in terms of $\bar{K}_{\alpha\gamma}^{(\beta)}$. Making these substitutions in Eqs. (C.4) and (C.5) give

$$\bar{n}^{(\beta)a} \gamma^b \bar{K}_{ab}^{(\alpha)} = \bar{N}^{(\beta)} (\bar{N}^{(\alpha)})^2 [\bar{g}^{\alpha\alpha} \bar{g}^{\beta\beta} - (\bar{g}^{\alpha\beta})^2] \bar{K}_{\beta\gamma}^{(\alpha)}, \quad (\text{C.6})$$

$$\bar{n}^{(\alpha)a} \gamma^b \bar{K}_{ab}^{(\beta)} = \bar{N}^{(\alpha)} (\bar{N}^{(\beta)})^2 [\bar{g}^{\alpha\alpha} \bar{g}^{\beta\beta} - (\bar{g}^{\alpha\beta})^2] \bar{K}_{\alpha\gamma}^{(\beta)}. \quad (\text{C.7})$$

It follows that the identity $\bar{n}^{(\alpha)a} \gamma^b \bar{K}_{ab}^{(\beta)} = -\bar{n}^{(\beta)a} \gamma^b \bar{K}_{ab}^{(\alpha)}$ from Eq. (C.1) implies the identity $\bar{N}^{(\beta)} \bar{K}_{\alpha\gamma}^{(\beta)} = -\bar{N}^{(\alpha)} \bar{K}_{\beta\gamma}^{(\alpha)}$ given in Eq. (45).

Appendix D. Example three-dimensional multicube manifolds

This appendix gives detailed descriptions of the multicube structures of several manifolds used in this study. New structures are presented here for all the examples constructed by hand (except the trivial flat examples, E2 and E3): the Poincaré dodecahedral space [11] in Table D.5, Seifert-Weber space [12] in Table D.7, $G_2 \times S^1$ in Table D.4, and the three non-trivial compact orientable three-manifolds that admit flat metrics [13,14], E4, E5 and E6 (Hantzsche-Wendt space [15]) in Tables D.1, D.2 and D.3 respectively. In addition, a selection of the multicube structures constructed automatically from triangulations using the code described in Appendix A are presented here: $KB/n2 \times \sim S^1$ in Table D.9, $L(5,2)$ in Table D.6, $SFS[RP2/n2:(2,1)(2,-1)]$ in Table D.10, and $SFS[S2:(2,1)(2,1)(2,-1)]$ in Table D.8.

The notation used to describe these multicube structures is based on that introduced in Ref. [1]. Each multicube structure consists of a set of non-overlapping cubes, \mathcal{B}_A , that cover the manifold, and a set of maps $\Psi_{B\beta}^{A\alpha}$ that identify the faces of neighboring cubes. The interface boundary maps used here (written in terms of the global Cartesian coordinates used for the multicube structure) take points, x_B^i , on the interface boundary $B\{\beta\}$ (or equivalently $\partial_\beta \mathcal{B}_B$) of region \mathcal{B}_B to the corresponding points, x_A^i , in the boundary $A\{\alpha\}$ (or equivalently $\partial_\alpha \mathcal{B}_A$) of region \mathcal{B}_A in the following way,

$$x_A^i = c_A^i + f_\alpha^i + C_{B\beta j}^{A\alpha i} (x_B^j - c_B^j - f_\beta^j). \tag{D.1}$$

The vectors $\vec{c}_A + \vec{f}_\alpha$ and $\vec{c}_B + \vec{f}_\beta$ are the locations of the centers of the $A\{\alpha\}$ and $B\{\beta\}$ faces respectively, and $C_{B\beta}^{A\alpha}$ is the combined rotation/reflection matrix needed to orient the faces properly.

The following tables include lists of the cubic regions, \mathcal{B}_A , used to cover the manifold in each structure, the vectors \vec{c}_A that define the locations of the centers of these regions in \mathbb{R}^3 , and the rotation/reflection matrices $C_{B\beta}^{A\alpha}$ needed to transform each cube face into the face of its neighbor.² The identification of the $B\{\beta\}$ face with the $A\{\alpha\}$ face is indicated in the tables by $\{\alpha A\} \leftrightarrow \{\beta B\}$. The notation **I** in these tables indicates the identity matrix, while \mathbf{R}_α indicates the $+\pi/2$ rotation about the outward directed normal to the $\{\alpha\}$ cube face.

Table D.1

Multi-Cube representation of Third-Turn space [13,14] (E4, one of the six compact orientable three-manifolds that admits a global flat metric), can be constructed by identifying opposite rectangular faces of a hexagonal cylinder, and identifying the two hexagonal faces after twisting by $2\pi/3$. Multi-cube structure: region center locations \vec{c}_A , region face identifications, $\{\alpha A\} \leftrightarrow \{\beta B\}$, and the rotation matrices for the associated interface maps, $C_{A\alpha}^{B\beta}$.

A	\vec{c}_A	$\alpha = -x$ $B \beta \ C_{A\alpha}^{B\beta}$	$\alpha = +x$ $B \beta \ C_{A\alpha}^{B\beta}$	$\alpha = -y$ $B \beta \ C_{A\alpha}^{B\beta}$	$\alpha = +y$ $B \beta \ C_{A\alpha}^{B\beta}$	$\alpha = -z$ $B \beta \ C_{A\alpha}^{B\beta}$	$\alpha = +z$ $B \beta \ C_{A\alpha}^{B\beta}$
1	(0, 0, 0)	$2+x \ \mathbf{I}$	$2-x \ \mathbf{I}$	$3+y \ \mathbf{I}$	$3-y \ \mathbf{I}$	$2+z \ \mathbf{R}_{+z}$	$3-z \ \mathbf{R}_{-z}$
2	(1, 0, 0)	$1+x \ \mathbf{I}$	$1-x \ \mathbf{I}$	$3-x \ \mathbf{R}_{+z}$	$3+x \ \mathbf{R}_{+z}$	$3+z \ \mathbf{R}_{+z}^2$	$1-z \ \mathbf{R}_{-z}$
3	(0, 1, 0)	$2-y \ \mathbf{R}_{-z}$	$2+y \ \mathbf{R}_{-z}$	$1+y \ \mathbf{I}$	$1-y \ \mathbf{I}$	$1+z \ \mathbf{R}_{+z}$	$2-z \ \mathbf{R}_{-z}^2$

Table D.2

Multi-Cube representation of Sixth-Turn space [13,14] (E5, one of the six compact orientable three-manifolds that admits a global flat metric), can be constructed by identifying opposite rectangular faces of a hexagonal cylinder, and identifying the two hexagonal faces after twisting by $2\pi/6$. Multi-cube structure: region center locations \vec{c}_A , region face identifications, $\{\alpha A\} \leftrightarrow \{\beta B\}$, and the rotation matrices for the associated interface maps, $C_{A\alpha}^{B\beta}$.

A	\vec{c}_A	$\alpha = -x$ $B \beta \ C_{A\alpha}^{B\beta}$	$\alpha = +x$ $B \beta \ C_{A\alpha}^{B\beta}$	$\alpha = -y$ $B \beta \ C_{A\alpha}^{B\beta}$	$\alpha = +y$ $B \beta \ C_{A\alpha}^{B\beta}$	$\alpha = -z$ $B \beta \ C_{A\alpha}^{B\beta}$	$\alpha = +z$ $B \beta \ C_{A\alpha}^{B\beta}$
1	(0, 1, 0)	$5-x \ \mathbf{R}_{+z}^2$	$6+y \ \mathbf{R}_{-z}$	$2+y \ \mathbf{I}$	$3+x \ \mathbf{R}_{+z}$	$2+z \ \mathbf{R}_{+z}$	$6-z \ \mathbf{R}_{+z}^2$
2	(0, 0, 0)	$4-x \ \mathbf{R}_{+z}^2$	$3-x \ \mathbf{I}$	$6-y \ \mathbf{R}_{+z}^2$	$1-y \ \mathbf{I}$	$3+z \ \mathbf{R}_{+z}$	$1-z \ \mathbf{R}_{-z}$
3	(1, 0, 0)	$2+x \ \mathbf{I}$	$1+y \ \mathbf{R}_{-z}$	$5-y \ \mathbf{R}_{+z}^2$	$4+x \ \mathbf{R}_{+z}$	$4+z \ \mathbf{R}_{+z}^2$	$2-z \ \mathbf{R}_{-z}$
4	(3, 1, 0)	$2-x \ \mathbf{R}_{+z}^2$	$3+y \ \mathbf{R}_{-z}$	$5+y \ \mathbf{I}$	$6+x \ \mathbf{R}_{+z}$	$5+z \ \mathbf{R}_{+z}$	$3-z \ \mathbf{R}_{+z}^2$
5	(3, 0, 0)	$1-x \ \mathbf{R}_{+z}^2$	$6-x \ \mathbf{I}$	$3-y \ \mathbf{R}_{+z}^2$	$4-y \ \mathbf{I}$	$6+z \ \mathbf{R}_{+z}$	$4-z \ \mathbf{R}_{-z}$
6	(4, 0, 0)	$5+x \ \mathbf{I}$	$4+y \ \mathbf{R}_{-z}$	$2-y \ \mathbf{R}_{+z}^2$	$1+x \ \mathbf{R}_{+z}$	$1+z \ \mathbf{R}_{+z}^2$	$5-z \ \mathbf{R}_{-z}$

² The vectors \vec{f}_α are the relative positions of the center of the $A\{\alpha\}$ cube face with the center of region \mathcal{B}_A . These vectors are the same for all the cubic regions, and are given explicitly in Ref. [1] so they are not repeated here.

Table D.3

Multi-Cube representation of Hantzsche-Wendt space [13–15] (E6, one of the six compact orientable three-manifolds that admits a global flat metric), can be constructed by identifying faces on two cubic regions (see Ref. [14] example 8.1.7 for details). Multicube structure: region center locations \tilde{c}_A , region face identifications, $\{\alpha A\} \rightarrow \{\beta B\}$, and the rotation matrices for the associated interface maps, $\mathbf{C}_{A\alpha}^{B\beta}$.

A	\tilde{c}_A	$\alpha = -x$ $B \beta \mathbf{C}_{A\alpha}^{B\beta}$	$\alpha = +x$ $B \beta \mathbf{C}_{A\alpha}^{B\beta}$	$\alpha = -y$ $B \beta \mathbf{C}_{A\alpha}^{B\beta}$	$\alpha = +y$ $B \beta \mathbf{C}_{A\alpha}^{B\beta}$	$\alpha = -z$ $B \beta \mathbf{C}_{A\alpha}^{B\beta}$	$\alpha = +z$ $B \beta \mathbf{C}_{A\alpha}^{B\beta}$
0	(0, 0, 0)	$1+x \mathbf{R}_{+x}^2$	$1-x \mathbf{R}_{+x}^2$	$1-y \mathbf{R}_{+z}^2$	$1+y \mathbf{R}_{+z}^2$	$1+z \mathbf{I}$	$1-z \mathbf{I}$
1	(0, 0, 1)	$0+x \mathbf{R}_{+x}^2$	$0-x \mathbf{R}_{+x}^2$	$0-y \mathbf{R}_{+z}^2$	$0+y \mathbf{R}_{+z}^2$	$0+z \mathbf{I}$	$0-z \mathbf{I}$

Table D.4

Multicube representation of the product space $G2 \times S1$ constructed from the genus number $N_g = 2$ two-dimensional compact orientable manifold. Multicube Structure: region center locations \tilde{c}_A , region face identifications, $\{\alpha A\} \leftrightarrow \{\beta B\}$, and the rotation matrices for the associated interface maps, $\mathbf{C}_{A\alpha}^{B\beta}$.

A	\tilde{c}_A	$\alpha = -x$ $B \beta \mathbf{C}_{A\alpha}^{B\beta}$	$\alpha = +x$ $B \beta \mathbf{C}_{A\alpha}^{B\beta}$	$\alpha = -y$ $B \beta \mathbf{C}_{A\alpha}^{B\beta}$	$\alpha = +y$ $B \beta \mathbf{C}_{A\alpha}^{B\beta}$	$\alpha = -z$ $B \beta \mathbf{C}_{A\alpha}^{B\beta}$	$\alpha = +z$ $B \beta \mathbf{C}_{A\alpha}^{B\beta}$
1	(L, 2L, 0)	$8+x \mathbf{I}$	$10-x \mathbf{I}$	$2+y \mathbf{I}$	$4-y \mathbf{I}$	$1+z \mathbf{I}$	$1-z \mathbf{I}$
2	(L, L, 0)	$7+x \mathbf{I}$	$4+x \mathbf{R}_{+z}^2$	$3+y \mathbf{I}$	$1-y \mathbf{I}$	$2+z \mathbf{I}$	$2-z \mathbf{I}$
3	(L, 0, 0)	$6+x \mathbf{I}$	$9-x \mathbf{I}$	$4+y \mathbf{I}$	$2-y \mathbf{I}$	$3+z \mathbf{I}$	$3-z \mathbf{I}$
4	(L, -L, 0)	$5+x \mathbf{I}$	$2+x \mathbf{R}_{-z}^2$	$1+y \mathbf{I}$	$3-y \mathbf{I}$	$4+z \mathbf{I}$	$4-z \mathbf{I}$
5	(0, -L, 0)	$7-x \mathbf{R}_{+z}^2$	$4-x \mathbf{I}$	$8+y \mathbf{I}$	$6-y \mathbf{I}$	$5+z \mathbf{I}$	$5-z \mathbf{I}$
6	(0, 0, 0)	$9+x \mathbf{I}$	$3-x \mathbf{I}$	$5+y \mathbf{I}$	$7-y \mathbf{I}$	$6+z \mathbf{I}$	$6-z \mathbf{I}$
7	(0, L, 0)	$5-x \mathbf{R}_{-z}^2$	$2-x \mathbf{I}$	$6+y \mathbf{I}$	$8-y \mathbf{I}$	$7+z \mathbf{I}$	$7-z \mathbf{I}$
8	(0, 2L, 0)	$10+x \mathbf{I}$	$1-x \mathbf{I}$	$7+y \mathbf{I}$	$5-y \mathbf{I}$	$8+z \mathbf{I}$	$8-z \mathbf{I}$
9	(-L, 0, 0)	$3+x \mathbf{I}$	$6-x \mathbf{I}$	$9+y \mathbf{I}$	$9-y \mathbf{I}$	$9+z \mathbf{I}$	$9-z \mathbf{I}$
10	(-L, 2L, 0)	$1+x \mathbf{I}$	$8-x \mathbf{I}$	$10+y \mathbf{I}$	$10-y \mathbf{I}$	$10+z \mathbf{I}$	$10-z \mathbf{I}$

Table D.5

Multicube representation of the Poincaré dodecahedral space (also called the Poincaré homology three-sphere) [11]. This multicube structure is based on cutting a dodecahedron into twenty cubes (each vertex of the dodecahedron is the vertex of one of the cubes, opposite vertices of these cubes all intersect at the center of the dodecahedron) and identifying opposite faces of the dodecahedron after rotation by $\pi/5$. Multicube Structure: region center locations \tilde{c}_A , region face identifications, $\{\alpha A\} \leftrightarrow \{\beta B\}$, and the rotation matrices for the associated interface maps, $\mathbf{C}_{A\alpha}^{B\beta}$.

A	\tilde{c}_A	$\alpha = -x$ $B \beta \mathbf{C}_{A\alpha}^{B\beta}$	$\alpha = +x$ $B \beta \mathbf{C}_{A\alpha}^{B\beta}$	$\alpha = -y$ $B \beta \mathbf{C}_{A\alpha}^{B\beta}$	$\alpha = +y$ $B \beta \mathbf{C}_{A\alpha}^{B\beta}$	$\alpha = -z$ $B \beta \mathbf{C}_{A\alpha}^{B\beta}$	$\alpha = +z$ $B \beta \mathbf{C}_{A\alpha}^{B\beta}$
1	(2L, 3L, 0)	$12+y \mathbf{R}_{+y} \mathbf{R}_{+z}$	$15-y \mathbf{R}_{+z}$	$8-y \mathbf{R}_{-y} \mathbf{R}_{+x}^2$	$4+x \mathbf{R}_{+x} \mathbf{R}_{+z}$	$10-y \mathbf{R}_{-y} \mathbf{R}_{+x}$	$2-z \mathbf{I}$
2	(2L, 3L, L)	$6+x \mathbf{I}$	$16-y \mathbf{R}_{+z}$	$18+y \mathbf{I}$	$13-z \mathbf{R}_{-z} \mathbf{R}_{+x}$	$1+z \mathbf{I}$	$7-z \mathbf{R}_{+z}$
3	(4L, 0, 3L)	$7+x \mathbf{I}$	$12+z \mathbf{R}_{+z} \mathbf{R}_{+y}$	$19+y \mathbf{I}$	$9-x \mathbf{R}_{-z}$	$18+z \mathbf{R}_{-z}$	$4-z \mathbf{I}$
4	(4L, 0, 4L)	$17-x \mathbf{R}_{+x} \mathbf{R}_{+z}^2$	$1+y \mathbf{R}_{-z} \mathbf{R}_{-x}$	$13+x \mathbf{R}_{+x} \mathbf{R}_{-z}$	$10-x \mathbf{R}_{-z}$	$3+z \mathbf{I}$	$15-x \mathbf{R}_{-x} \mathbf{R}_{+y}$
5	(0, 3L, 0)	$8+y \mathbf{R}_{+y} \mathbf{R}_{+z}$	$12+x \mathbf{R}_{+x} \mathbf{R}_{+y}^2$	$16+y \mathbf{R}_{+y}$	$19+x \mathbf{R}_{+z}$	$14-y \mathbf{R}_{+x}$	$6-z \mathbf{I}$
6	(0, 3L, L)	$17-z \mathbf{R}_{-z} \mathbf{R}_{+y}$	$2-x \mathbf{I}$	$10+y \mathbf{I}$	$20+x \mathbf{R}_{+z}$	$5+z \mathbf{I}$	$11-z \mathbf{R}_{+z}$
7	(2L, 3L, 3L)	$13-x \mathbf{R}_{+z}^2$	$3-x \mathbf{I}$	$11+y \mathbf{I}$	$16+z \mathbf{R}_{-x}$	$2+z \mathbf{R}_{-z}$	$8-z \mathbf{I}$
8	(2L, 3L, 4L)	$14-x \mathbf{R}_{+z}^2$	$17+y \mathbf{R}_{+y} \mathbf{R}_{-z}$	$1-y \mathbf{R}_{-x}^2 \mathbf{R}_{+y}$	$5-x \mathbf{R}_{-z} \mathbf{R}_{-y}$	$7+z \mathbf{I}$	$19-y \mathbf{R}_{-y} \mathbf{R}_{-x}$
9	(0, L, 0)	$3+y \mathbf{R}_{+z}$	$20-x \mathbf{R}_{-x}$	$12-x \mathbf{R}_{-x} \mathbf{R}_{+z}$	$16+x \mathbf{R}_{-x} \mathbf{R}_{+z}$	$18+x \mathbf{R}_{+y}$	$10-z \mathbf{I}$
10	(0, L, L)	$4+y \mathbf{R}_{+z}$	$14+y \mathbf{R}_{-z}$	$1-z \mathbf{R}_{-x} \mathbf{R}_{+y}$	$6-y \mathbf{I}$	$9+z \mathbf{I}$	$15-z \mathbf{I}$
11	(0, 3L, 3L)	$20+z \mathbf{R}_{-y}$	$15+y \mathbf{R}_{-z}$	$17-y \mathbf{R}_{+z}^2$	$7-y \mathbf{I}$	$6+z \mathbf{R}_{-z}$	$12-z \mathbf{I}$
12	(0, 3L, 4L)	$9-y \mathbf{R}_{-z} \mathbf{R}_{+x}$	$5+x \mathbf{R}_{-y}^2 \mathbf{R}_{-x}$	$18-y \mathbf{R}_{+z}^2$	$1-x \mathbf{R}_{-z} \mathbf{R}_{-y}$	$11+z \mathbf{I}$	$3+x \mathbf{R}_{-y} \mathbf{R}_{-z}$
13	(2L, 0, 0)	$7-x \mathbf{R}_{+z}^2$	$4-y \mathbf{R}_{+z} \mathbf{R}_{-x}$	$16-x \mathbf{R}_{-x} \mathbf{R}_{+z}$	$20+y \mathbf{R}_{-y} \mathbf{R}_{+z}^2$	$2+y \mathbf{R}_{-x} \mathbf{R}_{+z}$	$14-z \mathbf{I}$
14	(2L, 0, L)	$8-x \mathbf{R}_{+z}^2$	$18-x \mathbf{I}$	$5-z \mathbf{R}_{-x}$	$10+x \mathbf{R}_{+z}$	$13+z \mathbf{I}$	$19-z \mathbf{R}_{+z}$
15	(0, L, 3L)	$4+z \mathbf{R}_{-y} \mathbf{R}_{+x}$	$19-x \mathbf{I}$	$1+x \mathbf{R}_{-z}$	$11+x \mathbf{R}_{+z}$	$10+z \mathbf{I}$	$16-z \mathbf{I}$
16	(0, L, 4L)	$13-y \mathbf{R}_{-z} \mathbf{R}_{+x}$	$9+y \mathbf{R}_{-z} \mathbf{R}_{+x}$	$2+x \mathbf{R}_{-z}$	$5-y \mathbf{R}_{-y}$	$15+z \mathbf{I}$	$7+y \mathbf{R}_{+x}$
17	(4L, 0, 0)	$4-x \mathbf{R}_{+z}^2 \mathbf{R}_{-x}$	$20-y \mathbf{R}_{-y} \mathbf{R}_{+z}$	$11-y \mathbf{R}_{+z}^2$	$8+x \mathbf{R}_{+z} \mathbf{R}_{-y}$	$6-x \mathbf{R}_{-y} \mathbf{R}_{+z}$	$18-z \mathbf{I}$
18	(4L, 0, L)	$14+x \mathbf{I}$	$9-z \mathbf{R}_{-y}$	$12-y \mathbf{R}_{+z}^2$	$2-y \mathbf{I}$	$17+z \mathbf{I}$	$3-z \mathbf{R}_{+z}$
19	(2L, 0, 3L)	$15+x \mathbf{I}$	$5+y \mathbf{R}_{-z}$	$8+z \mathbf{R}_{+x} \mathbf{R}_{+y}$	$3-y \mathbf{I}$	$14+z \mathbf{R}_{-z}$	$20-z \mathbf{I}$
20	(2L, 0, 4L)	$9+x \mathbf{R}_{+x}$	$6+y \mathbf{R}_{-z}$	$17+x \mathbf{R}_{-z} \mathbf{R}_{+y}$	$13+y \mathbf{R}_{+z}^2 \mathbf{R}_{+y}$	$19+z \mathbf{I}$	$11-x \mathbf{R}_{+y}$

Table D.6

Multicube representation of the Regina triangulation of the lens space $L(5,2)$. Multicube Structure: region center locations \bar{c}_A , region face identifications, $\{\alpha A\} \leftrightarrow \{\beta B\}$, and the rotation matrices for the associated interface maps, $C_{A\alpha}^{B\beta}$.

A	\bar{c}_A	$\alpha = -x$ $B \beta C_{A\alpha}^{B\beta}$	$\alpha = +x$ $B \beta C_{A\alpha}^{B\beta}$	$\alpha = -y$ $B \beta C_{A\alpha}^{B\beta}$	$\alpha = +y$ $B \beta C_{A\alpha}^{B\beta}$	$\alpha = -z$ $B \beta C_{A\alpha}^{B\beta}$	$\alpha = +z$ $B \beta C_{A\alpha}^{B\beta}$
0.0	(0, 0, 0)	$0.3 + z R_{-y}R_{-x}$	$0.1 - x I$	$0.2 - z R_{-x}R_{+y}$	$0.2 - y I$	$0.1 - y R_{+x}R_{+z}$	$0.3 - z I$
0.1	(L, 0, 0)	$0.0 + x I$	$0.2 - x R_{+x}$	$0.0 - z R_{-x}R_{+y}$	$0.2 + x R_{+z}$	$0.3 - y R_{+z}R_{-x}$	$0.3 + x R_{-y}$
0.2	(0, L, 0)	$0.1 + x R_{-x}$	$0.1 + y R_{-z}$	$0.0 + y I$	$0.3 - x R_{+y}R_{+z}$	$0.0 - y R_{+x}R_{+z}$	$0.3 + y R_{+x}$
0.3	(0, 0, L)	$0.2 + y R_{+x}R_{-z}$	$0.1 + z R_{+y}$	$0.1 - z R_{+y}R_{+x}$	$0.2 + z R_{-x}$	$0.0 + z I$	$0.0 - x R_{+y}R_{+z}$

Table D.7

Multicube representation of Seifert-Weber space [12]. This multicube structure is based on cutting a dodecahedron into twenty cubes (each vertex of the dodecahedron is the vertex of one of the cubes, opposite vertices of these cubes all intersect at the center of the dodecahedron) and identifying opposite faces of the dodecahedron after rotation by $3\pi/5$. Multicube Structure: region center locations \bar{c}_A , region face identifications, $\{\alpha A\} \leftrightarrow \{\beta B\}$, and the rotation matrices for the associated interface maps, $C_{A\alpha}^{B\beta}$.

A	\bar{c}_A	$\alpha = -x$ $B \beta C_{A\alpha}^{B\beta}$	$\alpha = +x$ $B \beta C_{A\alpha}^{B\beta}$	$\alpha = -y$ $B \beta C_{A\alpha}^{B\beta}$	$\alpha = +y$ $B \beta C_{A\alpha}^{B\beta}$	$\alpha = -z$ $B \beta C_{A\alpha}^{B\beta}$	$\alpha = +z$ $B \beta C_{A\alpha}^{B\beta}$
1	(2L, 3L, 0)	$12 + y R_{+y}R_{+z}$	$19 - y R_{-y}R_{+z}$	$8 - y R_{-y}R_{+x}^2$	$13 - z R_{+z}R_{+x}$	$9 - y R_{+y}R_{+x}$	$2 - z I$
2	(2L, 3L, L)	$6 + x I$	$15 - y R_{-y}R_{+z}$	$18 + y I$	$20 + x R_{+x}R_{+z}$	$1 + z I$	$3 - z I$
3	(2L, 3L, 2L)	$7 + x I$	$5 + y R_{+y}R_{-z}$	$19 + y I$	$10 - x R_{-x}R_{-z}$	$2 + z I$	$4 - z I$
4	(2L, 3L, 3L)	$17 - x R_{+x}R_{+z}^2$	$12 + z R_{+z}R_{+y}$	$13 + x R_{+x}R_{-z}$	$6 - x R_{-x}R_{-z}$	$3 + z I$	$16 - x R_{+x}R_{+y}$
5	(0, 3L, 0)	$17 - z R_{+z}R_{+y}$	$12 + x R_{+x}R_{+z}^2$	$16 + y R_{+y}$	$3 + x R_{+z}R_{-y}$	$13 - y R_{-y}R_{+x}$	$6 - z I$
6	(0, 3L, L)	$4 + y R_{+z}R_{+x}$	$2 - x I$	$10 + y I$	$19 + x R_{+x}R_{+z}$	$5 + z I$	$7 - z I$
7	(0, 3L, 2L)	$14 - x R_{+x}R_{+z}^2$	$3 - x I$	$11 + y I$	$9 - x R_{-x}R_{-z}$	$6 + z I$	$8 - z I$
8	(0, 3L, 3L)	$10 - y R_{-y}R_{-z}$	$17 + y R_{+y}R_{-z}$	$1 - y R_{-x}R_{+y}$	$16 + z R_{+z}R_{-x}$	$7 + z I$	$20 - y R_{+y}R_{-x}$
9	(0, L, 0)	$7 + y R_{+z}R_{+x}$	$20 - x R_{-x}$	$1 - z R_{-x}R_{+z}^2$	$16 + x R_{-x}R_{+z}$	$17 + x R_{+x}R_{+y}$	$10 - z I$
10	(0, L, L)	$3 + y R_{+z}R_{+x}$	$14 + y R_{-z}$	$8 - x R_{+z}R_{+y}$	$6 - y I$	$9 + z I$	$11 - z I$
11	(0, L, 2L)	$13 - x R_{-x}R_{+z}^2$	$15 + y R_{-z}$	$18 - y R_{-y}R_{+z}^2$	$7 - y I$	$10 + z I$	$12 - z I$
12	(0, L, 3L)	$20 + z R_{+z}R_{-y}$	$5 + x R_{+z}R_{-x}$	$14 - y R_{-y}R_{+z}^2$	$14 - y R_{-y}R_{-y}$	$11 + z I$	$4 + x R_{-y}R_{+z}^2$
13	(2L, 0, 0)	$11 - x R_{+z}R_{+x}$	$4 - y R_{+z}R_{-x}$	$5 - z R_{-x}R_{+y}$	$20 + y R_{-y}R_{+z}^2$	$1 + y R_{-x}R_{-z}$	$14 - z I$
14	(2L, 0, L)	$7 - x R_{+z}R_{-x}$	$18 - x I$	$12 - y R_{+z}R_{+y}$	$10 + x R_{+z}$	$13 + z I$	$15 - z I$
15	(2L, 0, 2L)	$17 - y R_{-y}R_{-z}$	$19 - x I$	$2 + x R_{-z}R_{+y}$	$11 + x R_{+z}$	$14 + z I$	$16 - z I$
16	(2L, 0, 3L)	$4 + z R_{-y}R_{+z}^2$	$9 + y R_{-z}R_{+x}$	$18 + x R_{+x}R_{-z}$	$5 - y R_{-y}$	$15 + z I$	$8 + y R_{+z}R_{-x}$
17	(4L, 0, 0)	$4 - x R_{+z}R_{-x}$	$9 - z R_{-y}R_{-x}$	$15 - x R_{+z}R_{+y}$	$8 + x R_{+z}R_{-y}$	$5 - x R_{-y}R_{+z}^2$	$18 - z I$
18	(4L, 0, L)	$14 + x I$	$16 - y R_{+z}R_{-x}$	$11 - y R_{+z}R_{+y}$	$2 - y I$	$17 + z I$	$19 - z I$
19	(4L, 0, 2L)	$15 + x I$	$6 + y R_{-z}R_{-x}$	$1 + x R_{-z}R_{+y}$	$3 - y I$	$18 + z I$	$20 - z I$
20	(4L, 0, 3L)	$9 + x R_{+x}$	$2 + y R_{-z}R_{-x}$	$8 + x R_{+x}R_{+z}^2$	$13 + y R_{+z}R_{+y}$	$19 + z I$	$12 - x R_{+y}R_{-z}$

Table D.8

Multicube representation of the Regina triangulation of the Seifert fiber space $SFS[S2;(2,1)(2,1)(2,-1)]$. Multicube Structure: region center locations \bar{c}_A , region face identifications, $\{\alpha A\} \leftrightarrow \{\beta B\}$, and the rotation matrices for the associated interface maps, $C_{A\alpha}^{B\beta}$.

A	\bar{c}_A	$\alpha = -x$ $B \beta C_{A\alpha}^{B\beta}$	$\alpha = +x$ $B \beta C_{A\alpha}^{B\beta}$	$\alpha = -y$ $B \beta C_{A\alpha}^{B\beta}$	$\alpha = +y$ $B \beta C_{A\alpha}^{B\beta}$	$\alpha = -z$ $B \beta C_{A\alpha}^{B\beta}$	$\alpha = +z$ $B \beta C_{A\alpha}^{B\beta}$
0.0	(0, 0, 0)	$1.2 - x R_{+z}^2$	$0.1 - x I$	$1.1 - z R_{-x}R_{-y}$	$0.2 - y I$	$1.3 - y R_{+x}R_{-z}$	$0.3 - z I$
0.1	(L, 0, 0)	$0.0 + x I$	$1.3 + z R_{+y}$	$1.2 - z R_{+z}R_{+x}$	$0.2 + x R_{+z}$	$1.0 - y R_{+x}R_{-z}$	$0.3 + x R_{-y}$
0.2	(0, L, 0)	$1.0 - x R_{+z}^2$	$0.1 + y R_{-z}$	$0.0 + y I$	$1.2 + y R_{+z}R_{+y}$	$1.1 - y R_{+z}R_{-x}$	$0.3 + y R_{+x}$
0.3	(0, 0, L)	$1.3 - x R_{+z}^2R_{-x}$	$0.1 + z R_{+y}$	$1.0 - z R_{-x}R_{-y}$	$0.2 + z R_{-x}$	$0.0 + z I$	$1.1 + x R_{-y}$
1.0	(3L, 0, 0)	$0.2 - x R_{+z}^2$	$1.1 - x I$	$0.1 - z R_{-x}R_{-y}$	$1.2 - y I$	$0.3 - y R_{+x}R_{-z}$	$1.3 - z I$
1.1	(4L, 0, 0)	$1.0 + x I$	$0.3 + z R_{+y}$	$0.2 - z R_{+z}R_{+x}$	$1.2 + x R_{+z}$	$0.0 - y R_{+x}R_{-z}$	$1.3 + x R_{-y}$
1.2	(3L, L, 0)	$0.0 - x R_{+z}^2$	$1.1 + y R_{-z}$	$1.0 + y I$	$0.2 + y R_{+z}R_{+y}$	$0.1 - y R_{+z}R_{-x}$	$1.3 + y R_{+x}$
1.3	(3L, 0, L)	$0.3 - x R_{+z}^2R_{-x}$	$1.1 + z R_{+y}$	$0.0 - z R_{-x}R_{-y}$	$1.2 + z R_{-x}$	$1.0 + z I$	$0.1 + x R_{-y}$

References

- [1] L. Lindblom, B. Szilágyi, Solving partial differential equations numerically on manifolds with arbitrary spatial topologies, *J. Comput. Phys.* 243 (2013) 151–175.
- [2] S.V. Matveev, Tabulation of three-dimensional manifolds, *Russ. Math. Surv.* 60 (2005) 673–698.
- [3] B. Martelli, C. Petronio, 3-manifolds having complexity at most 9, *Exp. Math.* 10 (2001) 207–237.
- [4] B. Martelli, C. Petronio, Complexity of 3-manifolds, in: *Spaces of Kleinian Groups*, in: London Math. Soc. Lecture Note Ser., vol. 329, Cambridge Univ. Press, 2006, pp. 91–120.
- [5] B.A. Burton, Detecting genus in vertex links for the fast enumeration of 3-manifold triangulations, in: *ISSAC 2011: Proceedings of the 36th International Symposium on Symbolic and Algebraic Computation*, ACM, 2011, pp. 527–571.
- [6] B.A. Burton, R. Budney, W. Pettersson, et al., Regina: software for low-dimensional topology, <http://regina-normal.github.io/>, 1999–2021.

Table D.9

Multicube representation of the Regina triangulation of the Seifert fiber space $KB/n2 \times \sim S1$. Multicube Structure: region center locations \bar{c}_A , region face identifications, $\{\alpha A\} \leftrightarrow \{\beta B\}$, and the rotation matrices for the associated interface maps, $C_{A\alpha}^{\beta\beta}$.

A	\bar{c}_A	$\alpha = -x$ $B \beta C_{A\alpha}^{\beta\beta}$	$\alpha = +x$ $B \beta C_{A\alpha}^{\beta\beta}$	$\alpha = -y$ $B \beta C_{A\alpha}^{\beta\beta}$	$\alpha = +y$ $B \beta C_{A\alpha}^{\beta\beta}$	$\alpha = -z$ $B \beta C_{A\alpha}^{\beta\beta}$	$\alpha = +z$ $B \beta C_{A\alpha}^{\beta\beta}$
0.0	(0, 0, 0)	$2.1 + x \mathbf{I}$	$0.1 - x \mathbf{I}$	$3.1 + x \mathbf{R}_{-z} \mathbf{R}_{-y}$	$0.2 - y \mathbf{I}$	$4.3 + z \mathbf{I}$	$0.3 - z \mathbf{I}$
0.1	(L, 0, 0)	$0.0 + x \mathbf{I}$	$1.1 + x \mathbf{R}_{+z}^2 \mathbf{R}_{+x}$	$3.3 + z \mathbf{R}_{+y}^2 \mathbf{R}_{-x}$	$0.2 + x \mathbf{R}_{+z}$	$4.1 + x \mathbf{R}_{+y}$	$0.3 + x \mathbf{R}_{-y}$
0.2	(0, L, 0)	$2.2 + y \mathbf{R}_{+z}$	$0.1 + y \mathbf{R}_{-z}$	$0.0 + y \mathbf{I}$	$1.3 + z \mathbf{R}_{-x}$	$4.2 + y \mathbf{R}_{-x}$	$0.3 + y \mathbf{R}_{-x}$
0.3	(0, 0, L)	$2.3 + z \mathbf{R}_{-y}$	$0.1 + z \mathbf{R}_{+y}$	$3.2 + y \mathbf{R}_{-y}$	$0.2 + z \mathbf{R}_{-x}$	$0.0 + z \mathbf{I}$	$1.2 + y \mathbf{R}_{+x}$
1.0	(0, 3L, 0)	$2.2 - x \mathbf{R}_{+z}^2$	$1.1 - x \mathbf{I}$	$5.2 + y \mathbf{I}$	$1.2 - y \mathbf{I}$	$3.3 - x \mathbf{R}_{-y} \mathbf{R}_{+z}$	$1.3 - z \mathbf{I}$
1.1	(L, 3L, 0)	$1.0 + x \mathbf{I}$	$0.1 + x \mathbf{R}_{+z}^2 \mathbf{R}_{+x}$	$5.1 + x \mathbf{R}_{-z}$	$1.2 + x \mathbf{R}_{+z}$	$3.2 - x \mathbf{R}_{+z}^2 \mathbf{R}_{+y}$	$1.3 + x \mathbf{R}_{-y}$
1.2	(0, 4L, 0)	$2.0 - x \mathbf{R}_{+z}^2$	$1.1 + y \mathbf{R}_{-z}$	$1.0 + y \mathbf{I}$	$0.3 + z \mathbf{R}_{-x}$	$3.0 - x \mathbf{R}_{-y} \mathbf{R}_{+z}$	$1.3 + y \mathbf{R}_{+x}$
1.3	(0, 3L, L)	$2.3 - x \mathbf{R}_{+z}^2 \mathbf{R}_{-x}$	$1.1 + z \mathbf{R}_{+y}$	$5.3 + z \mathbf{R}_{+x}$	$1.2 + z \mathbf{R}_{-x}$	$1.0 + z \mathbf{I}$	$0.2 + y \mathbf{R}_{+x}$
2.0	(3L, 0, 0)	$1.2 - x \mathbf{R}_{+z}^2$	$2.1 - x \mathbf{I}$	$5.3 - x \mathbf{R}_{+z} \mathbf{R}_{+y}$	$2.2 - y \mathbf{I}$	$4.3 - x \mathbf{R}_{-y} \mathbf{R}_{+z}$	$2.3 - z \mathbf{I}$
2.1	(4L, 0, 0)	$2.0 + x \mathbf{I}$	$0.0 - x \mathbf{I}$	$5.0 - x \mathbf{R}_{+z} \mathbf{R}_{+y}$	$2.2 + x \mathbf{R}_{+z}$	$4.2 - x \mathbf{R}_{+z}^2 \mathbf{R}_{+y}$	$2.3 + x \mathbf{R}_{-y}$
2.2	(3L, L, 0)	$1.0 - x \mathbf{R}_{+z}^2$	$2.1 + y \mathbf{R}_{-z}$	$2.0 + y \mathbf{I}$	$0.2 - x \mathbf{R}_{-z}$	$4.0 - x \mathbf{R}_{-y} \mathbf{R}_{+z}$	$2.3 + y \mathbf{R}_{+z}$
2.3	(3L, 0, L)	$1.3 - x \mathbf{R}_{+z}^2 \mathbf{R}_{-x}$	$2.1 + z \mathbf{R}_{+y}$	$5.2 - x \mathbf{R}_{+y}^2 \mathbf{R}_{-z}$	$2.2 + z \mathbf{R}_{-x}$	$2.0 + z \mathbf{I}$	$0.3 - x \mathbf{R}_{+y}$
3.0	(3L, 3L, 0)	$1.2 - z \mathbf{R}_{+y} \mathbf{R}_{+x}$	$3.1 - x \mathbf{I}$	$4.3 - y \mathbf{R}_{+x}^2$	$3.2 - y \mathbf{I}$	$5.1 - z \mathbf{R}_{+y}^2$	$3.3 - z \mathbf{I}$
3.1	(4L, 3L, 0)	$3.0 + x \mathbf{I}$	$0.0 - y \mathbf{R}_{+z} \mathbf{R}_{+x}$	$4.1 - y \mathbf{R}_{+z}^2 \mathbf{R}_{-y}$	$3.2 + x \mathbf{R}_{+z}$	$5.0 - z \mathbf{R}_{+y}^2$	$3.3 + x \mathbf{R}_{-y}$
3.2	(3L, 4L, 0)	$1.1 - z \mathbf{R}_{+x}^2 \mathbf{R}_{-y}$	$3.1 + y \mathbf{R}_{-z}$	$3.1 + y \mathbf{R}_{-z}$	$0.3 - y \mathbf{R}_{+y}$	$5.2 - z \mathbf{R}_{+y}^2 \mathbf{R}_{-z}$	$3.3 + y \mathbf{R}_{+x}$
3.3	(3L, 3L, L)	$1.0 - z \mathbf{R}_{+y} \mathbf{R}_{+x}$	$3.1 + z \mathbf{R}_{+y}$	$4.0 - y \mathbf{R}_{+x}^2$	$3.2 + z \mathbf{R}_{-x}$	$3.0 + z \mathbf{I}$	$0.1 - y \mathbf{R}_{+z}^2 \mathbf{R}_{+x}$
4.0	(6L, 0, 0)	$2.2 - z \mathbf{R}_{+y} \mathbf{R}_{+x}$	$4.1 - x \mathbf{I}$	$3.3 - y \mathbf{R}_{+x}^2$	$4.2 - y \mathbf{I}$	$5.0 - y \mathbf{R}_{+x}$	$4.3 - z \mathbf{I}$
4.1	(7L, 0, 0)	$4.0 + x \mathbf{I}$	$0.1 - z \mathbf{R}_{-y}$	$3.1 - y \mathbf{R}_{+x}^2 \mathbf{R}_{-y}$	$4.2 + x \mathbf{R}_{+z}$	$5.1 - y \mathbf{R}_{+x}$	$4.3 + x \mathbf{R}_{-y}$
4.2	(6L, L, 0)	$2.1 - z \mathbf{R}_{+x}^2 \mathbf{R}_{-y}$	$4.1 + y \mathbf{R}_{-z}$	$4.0 + y \mathbf{I}$	$0.2 - z \mathbf{R}_{+x}$	$5.3 - y \mathbf{R}_{+x}$	$4.3 + y \mathbf{R}_{+x}$
4.3	(6L, 0, L)	$2.0 - z \mathbf{R}_{+y} \mathbf{R}_{+x}$	$4.1 + z \mathbf{R}_{+y}$	$3.0 - y \mathbf{R}_{+x}^2$	$4.2 + z \mathbf{R}_{-x}$	$4.0 + z \mathbf{I}$	$0.0 - z \mathbf{I}$
5.0	(6L, 3L, 0)	$2.1 - y \mathbf{R}_{-z} \mathbf{R}_{+x}$	$5.1 - x \mathbf{I}$	$4.0 - z \mathbf{R}_{-x}$	$5.2 - y \mathbf{I}$	$3.1 - z \mathbf{R}_{+y}^2$	$5.3 - z \mathbf{I}$
5.1	(7L, 3L, 0)	$5.0 + x \mathbf{I}$	$1.1 - y \mathbf{R}_{+z}$	$4.1 - z \mathbf{R}_{-x}$	$5.2 + x \mathbf{R}_{+z}$	$3.0 - z \mathbf{R}_{+y}^2$	$5.3 + x \mathbf{R}_{-y}$
5.2	(6L, 4L, 0)	$2.3 - y \mathbf{R}_{+x}^2 \mathbf{R}_{+z}$	$5.1 + y \mathbf{R}_{-z}$	$5.0 + y \mathbf{I}$	$1.0 - y \mathbf{I}$	$3.2 - z \mathbf{R}_{+y}^2 \mathbf{R}_{-z}$	$5.3 + y \mathbf{R}_{+x}$
5.3	(6L, 3L, L)	$2.0 - y \mathbf{R}_{-z} \mathbf{R}_{+x}$	$5.1 + z \mathbf{R}_{+y}$	$4.2 - z \mathbf{R}_{-x}$	$5.2 + z \mathbf{R}_{-x}$	$5.0 + z \mathbf{I}$	$1.3 - y \mathbf{R}_{-x}$

Table D.10

Multicube representation of the Regina triangulation of the Seifert fiber space $SFS[RP2/n2:(2,1)(2,-1)]$. Multicube Structure: region center locations \bar{c}_A , region face identifications, $\{\alpha A\} \leftrightarrow \{\beta B\}$, and the rotation matrices for the associated interface maps, $C_{A\alpha}^{\beta\beta}$.

A	\bar{c}_A	$\alpha = -x$ $B \beta C_{A\alpha}^{\beta\beta}$	$\alpha = +x$ $B \beta C_{A\alpha}^{\beta\beta}$	$\alpha = -y$ $B \beta C_{A\alpha}^{\beta\beta}$	$\alpha = +y$ $B \beta C_{A\alpha}^{\beta\beta}$	$\alpha = -z$ $B \beta C_{A\alpha}^{\beta\beta}$	$\alpha = +z$ $B \beta C_{A\alpha}^{\beta\beta}$
0.0	(0, 0, 0)	$2.1 + x \mathbf{I}$	$0.1 - x \mathbf{I}$	$3.1 + x \mathbf{R}_{-z} \mathbf{R}_{-y}$	$0.2 - y \mathbf{I}$	$4.2 + y \mathbf{R}_{-x} \mathbf{R}_{-z}$	$0.3 - z \mathbf{I}$
0.1	(L, 0, 0)	$0.0 + x \mathbf{I}$	$1.1 + x \mathbf{R}_{+z}^2 \mathbf{R}_{+x}$	$3.3 + z \mathbf{R}_{+y}^2 \mathbf{R}_{-x}$	$0.2 + x \mathbf{R}_{+z}$	$4.3 + z \mathbf{R}_{-z}$	$0.3 + x \mathbf{R}_{-y}$
0.2	(0, L, 0)	$2.2 + y \mathbf{R}_{+z}$	$0.1 + y \mathbf{R}_{-z}$	$0.0 + y \mathbf{I}$	$1.3 + z \mathbf{R}_{-x}$	$4.1 + x \mathbf{R}_{+z}^2 \mathbf{R}_{-y}$	$0.3 + y \mathbf{R}_{+x}$
0.3	(0, 0, L)	$2.3 + z \mathbf{R}_{-y}$	$0.1 + z \mathbf{R}_{+y}$	$3.2 + y \mathbf{R}_{-y}$	$0.2 + z \mathbf{R}_{-x}$	$0.0 + z \mathbf{I}$	$1.2 + y \mathbf{R}_{+x}$
1.0	(0, 3L, 0)	$2.2 - x \mathbf{R}_{+z}^2$	$1.1 - x \mathbf{I}$	$5.2 + y \mathbf{I}$	$1.2 - y \mathbf{I}$	$3.3 - x \mathbf{R}_{-y} \mathbf{R}_{+z}$	$1.3 - z \mathbf{I}$
1.1	(L, 3L, 0)	$1.0 + x \mathbf{I}$	$0.1 + x \mathbf{R}_{+z}^2 \mathbf{R}_{+x}$	$5.1 + x \mathbf{R}_{-z}$	$1.2 + x \mathbf{R}_{+z}$	$3.2 - x \mathbf{R}_{+z}^2 \mathbf{R}_{+y}$	$1.3 + x \mathbf{R}_{-y}$
1.2	(0, 4L, 0)	$2.0 - x \mathbf{R}_{+z}^2$	$1.1 + y \mathbf{R}_{-z}$	$1.0 + y \mathbf{I}$	$0.3 + z \mathbf{R}_{-x}$	$3.0 - x \mathbf{R}_{-y} \mathbf{R}_{+z}$	$1.3 + y \mathbf{R}_{+x}$
1.3	(0, 3L, L)	$2.3 - x \mathbf{R}_{+z}^2 \mathbf{R}_{-x}$	$1.1 + z \mathbf{R}_{+y}$	$5.3 + z \mathbf{R}_{+x}$	$1.2 + z \mathbf{R}_{-x}$	$1.0 + z \mathbf{I}$	$0.2 + y \mathbf{R}_{+x}$
2.0	(3L, 0, 0)	$1.2 - x \mathbf{R}_{+z}^2$	$2.1 - x \mathbf{I}$	$5.3 - x \mathbf{R}_{+z} \mathbf{R}_{+y}$	$2.2 - y \mathbf{I}$	$4.0 - x \mathbf{R}_{-y}$	$2.3 - z \mathbf{I}$
2.1	(4L, 0, 0)	$2.0 + x \mathbf{I}$	$0.0 - x \mathbf{I}$	$5.0 - x \mathbf{R}_{+z} \mathbf{R}_{+y}$	$2.2 + x \mathbf{R}_{+z}$	$4.3 - x \mathbf{R}_{-y}$	$2.3 + x \mathbf{R}_{-y}$
2.2	(3L, L, 0)	$1.0 - x \mathbf{R}_{+z}^2$	$2.1 + y \mathbf{R}_{-z}$	$2.0 + y \mathbf{I}$	$0.2 - x \mathbf{R}_{-z}$	$4.2 - x \mathbf{R}_{-y}$	$2.3 + y \mathbf{R}_{+x}$
2.3	(3L, 0, L)	$1.3 - x \mathbf{R}_{+z}^2 \mathbf{R}_{-x}$	$2.1 + z \mathbf{R}_{+y}$	$5.2 - x \mathbf{R}_{+y}^2 \mathbf{R}_{-z}$	$2.2 + z \mathbf{R}_{-x}$	$2.0 + z \mathbf{I}$	$0.3 - x \mathbf{R}_{+y}$
3.0	(3L, 3L, 0)	$1.2 - z \mathbf{R}_{+y} \mathbf{R}_{+x}$	$3.1 - x \mathbf{I}$	$4.0 - z \mathbf{R}_{-x}$	$3.2 - y \mathbf{I}$	$5.1 - z \mathbf{R}_{+y}^2$	$3.3 - z \mathbf{I}$
3.1	(4L, 3L, 0)	$3.0 + x \mathbf{I}$	$0.0 - y \mathbf{R}_{+z} \mathbf{R}_{+x}$	$4.1 - z \mathbf{R}_{-x}$	$3.2 + x \mathbf{R}_{+z}$	$5.0 - z \mathbf{R}_{+y}^2$	$3.3 + x \mathbf{R}_{-y}$
3.2	(3L, 4L, 0)	$1.1 - z \mathbf{R}_{+x}^2 \mathbf{R}_{-y}$	$3.1 + y \mathbf{R}_{-z}$	$3.0 + y \mathbf{I}$	$0.3 - y \mathbf{R}_{+y}$	$5.2 - z \mathbf{R}_{+y}^2 \mathbf{R}_{-z}$	$3.3 + y \mathbf{R}_{+x}$
3.3	(3L, 3L, L)	$1.0 - z \mathbf{R}_{+y} \mathbf{R}_{+x}$	$3.1 + z \mathbf{R}_{+y}$	$4.2 - z \mathbf{R}_{-x}$	$3.2 + z \mathbf{R}_{-x}$	$3.0 + z \mathbf{I}$	$0.1 - y \mathbf{R}_{+z}^2 \mathbf{R}_{+x}$
4.0	(6L, 0, 0)	$2.0 - z \mathbf{R}_{+y}$	$4.1 - x \mathbf{I}$	$5.0 - y \mathbf{R}_{+x}^2 \mathbf{R}_{+y}$	$4.2 - y \mathbf{I}$	$3.0 - y \mathbf{R}_{+x}$	$4.3 - z \mathbf{I}$
4.1	(7L, 0, 0)	$4.0 + x \mathbf{I}$	$0.2 - z \mathbf{R}_{+x}^2 \mathbf{R}_{+y}$	$5.3 - y \mathbf{R}_{+x}^2 \mathbf{R}_{+y}$	$4.2 + x \mathbf{R}_{+z}$	$3.1 - y \mathbf{R}_{+x}$	$4.3 + x \mathbf{R}_{-y}$
4.2	(6L, L, 0)	$2.2 - z \mathbf{R}_{+y}$	$4.1 + y \mathbf{R}_{-z}$	$4.0 + y \mathbf{I}$	$0.0 - z \mathbf{R}_{+x} \mathbf{R}_{+y}$	$3.3 - y \mathbf{R}_{+x}$	$4.3 + y \mathbf{R}_{+x}$
4.3	(6L, 0, L)	$2.1 - z \mathbf{R}_{+y}$	$4.1 + z \mathbf{R}_{+y}$	$5.1 - y \mathbf{R}_{+x}^2 \mathbf{R}_{+y}$	$4.2 + z \mathbf{R}_{-x}$	$4.0 + z \mathbf{I}$	$0.1 - z \mathbf{R}_{+z}$
5.0	(6L, 3L, 0)	$2.1 - y \mathbf{R}_{-z} \mathbf{R}_{+x}$	$5.1 - x \mathbf{I}$	$4.0 - y \mathbf{R}_{+x}^2 \mathbf{R}_{+y}$	$5.2 - y \mathbf{I}$	$3.1 - z \mathbf{R}_{+y}^2$	$5.3 - z \mathbf{I}$
5.1	(7L, 3L, 0)	$5.0 + x \mathbf{I}$	$1.1 - y \mathbf{R}_{+z}$	$4.3 - y \mathbf{R}_{+x}^2 \mathbf{R}_{+y}$	$5.2 + x \mathbf{R}_{+z}$	$3.0 - z \mathbf{R}_{+y}^2$	$5.3 + x \mathbf{R}_{-y}$
5.2	(6L, 4L, 0)	$2.3 - y \mathbf{R}_{+x}^2 \mathbf{R}_{+z}$	$5.1 + y \mathbf{R}_{-z}$	$5.0 + y \mathbf{I}$	$1.0 - y \mathbf{I}$	$3.2 - z \mathbf{R}_{+y}^2 \mathbf{R}_{-z}$	$5.3 + y \mathbf{R}_{+x}$
5.3	(6L, 3L, L)	$2.0 - y \mathbf{R}_{-z} \mathbf{R}_{+x}$	$5.1 + z \mathbf{R}_{+y}$	$4.1 - y \mathbf{R}_{+x}^2 \mathbf{R}_{+y}$	$5.2 + z \mathbf{R}_{-x}$	$5.0 + z \mathbf{I}$	$1.3 - y \mathbf{R}_{-x}$

[7] L. Lindblom, N.W. Taylor, O. Rinne, Constructing reference metrics on multicube representations of arbitrary manifolds, *J. Comput. Phys.* 313 (2016) 31–56.
 [8] W. Israel, Singular hypersurfaces and thin shells in general relativity, *Nuovo Cimento* 44B (1966) 1–14. Erratum: 48B (1967) 463.
 [9] W.P. Thurston, *Three-Dimensional Geometry and Topology*, Princeton University Press, 1997.
 [10] P. Scott, The geometry of 3-manifolds, *Bull. Lond. Math. Soc.* 15 (1983) 401–487.

- [11] W. Threlfall, H. Seifert, Topologische Untersuchung der Diskontinuitätsbereiche endlicher Bewegungsgruppen des dreidimensionalen sphärischen Raumes, *Math. Ann.* 104 (1931) 1–70.
- [12] C. Weber, H. Seifert, Die beiden Dodekaederräume, *Math. Z.* 37 (1933) 237–253.
- [13] A. Riazuelo, J. Weeks, J.-P. Urzan, R. Lehoucq, J.-P. Luminet, Cosmic microwave background anisotropies in multiconnected flat spaces, *Phys. Rev. D* 69 (2004) 103518.
- [14] M.P. Hitchman, *Geometry with an introduction to cosmic topology*, <https://mphitchman.com/geometry/>, 2018.
- [15] W. Hantzsche, H. Wendt, Dreidimensionale euklidische Raumformen, *Math. Ann.* 110 (1934) 593–611.
- [16] A. Barton, S. Mayboroda, Boundary-value problems for higher-order elliptic equations in non-smooth domains, *Oper. Theory, Adv. Appl.* 236 (2014) 53–93.
- [17] B. Martelli, C. Petronio, *Three-manifolds up to complexity 10*, http://people.dm.unipi.it/petronio/files/3D/c9/c9_census.html, 2001.
- [18] L.E. Kidder, M.A. Scheel, S.A. Teukolsky, E.D. Carlson, G.B. Cook, Black hole evolution by spectral methods, *Phys. Rev. D* 62 (2000) 084032.
- [19] M.A. Scheel, H.P. Pfeiffer, L. Lindblom, L.E. Kidder, O. Rinne, S.A. Teukolsky, Solving Einstein's equations with dual coordinate frames, *Phys. Rev. D* 74 (2006) 104006.
- [20] B. Szilágyi, L. Lindblom, M.A. Scheel, Simulations of binary black hole mergers using spectral methods, *Phys. Rev. D* 80 (2009) 124010.
- [21] B. Chow, D. Knopf, *The Ricci Flow: An Introduction*, *Mathematical Surveys and Monographs*, vol. 110, Amer. Math. Soc., 2004.
- [22] R.S. Hamilton, The Ricci flow on surfaces, in: *Mathematics and General Relativity*, in: *Contemp. Math.*, vol. 71, Amer. Math. Soc., 1988, pp. 237–262.
- [23] B. Chow, The Ricci flow on the 2-sphere, *J. Differ. Geom.* 33 (1991) 325–334.
- [24] X. Chen, P. Lu, G. Tian, A note on uniformization of Riemann surfaces by Ricci flow, *Proc. Am. Math. Soc.* 134 (2006) 3391–3393.
- [25] D. DeTurck, Deforming metrics in the direction of their Ricci tensors, *J. Differ. Geom.* 17 (1983) 255–306.
- [26] J. Bemelmans, M. Min-Oo, E. Ruh, Smoothing Riemannian metrics, *Math. Z.* 188 (1984) 69–74.
- [27] S. Bando, Real analyticity of solutions of Hamilton's equation, *Math. Z.* 195 (1987) 93–97.
- [28] D. Garfinkle, J. Isenberg, The modeling of degenerate neck pinch singularities in Ricci flow by Bryant solitons, *J. Math. Phys.* 49 (2008) 073505.
- [29] L. Lindblom, B. Szilágyi, N.W. Taylor, Solving Einstein's equation numerically on manifolds with arbitrary spatial topologies, *Phys. Rev. D* 89 (2014) 044044.
- [30] J.L. Friedman, K. Schleich, D.M. Witt, Topological censorship, *Phys. Rev. Lett.* 75 (1995) 1872.
- [31] M. Eichmair, G.J. Galloway, D. Pollack, Topological censorship from the initial data point of view, *J. Differ. Geom.* 95 (2013) 389–405.
- [32] G. Galloway, *Topology and general relativity*, <https://www.math.miami.edu/~galloway/ESI2017.pdf>, 2017.
- [33] J.P. Boyd, *Chebyshev and Fourier Spectral Methods*, Dover Publications, 2000.
- [34] Y. Saad, M.H. Schultz, GMRES: a generalized minimal residual algorithm for solving nonsymmetric linear systems, *SIAM J. Sci. Stat. Comput.* 7 (1986) 856–869.
- [35] H.A. Van Der Vorst, BI-CGSTAB: a fast and smoothly converging variant of BI-CG for the solution of nonsymmetric linear systems, *SIAM J. Sci. Stat. Comput.* 13 (1992) 631–644.
- [36] W.H. Press, S.A. Teukolsky, W.T. Vetterling, B.P. Flannery, *Numerical Recipes*, second edition, Cambridge University Press, 1992.
- [37] A.K. Cline, C.B. Moler, G.W. Stewart, J.H. Wilkinson, An estimate for the condition number of a matrix, *SIAM J. Numer. Anal.* 16 (1979) 369–375.